NON-UNIFORM RATIONAL B-SPLINE BASED ISO-GEOMETRIC ANALYSIS FOR A CLASS OF HYDRODYNAMIC PROBLEMS

(DOI No: 10.3940/rina.ijme.2020.a2.591)

M Goel, Cybermarine Knowledge System Private Limited, India, **R Sharma**, Design and Simulation Laboratory, Department of Ocean Engineering, IIT Madras, India, **S K Bhattacharyya**, Department of Ocean Engineering, IIT Madras, India and **Tae-wan Kim**, Department of Naval Architecture and Ocean Engineering, and Research Institute of Marine Systems Engineering, Seoul National University, Republic of Korea

SUMMARY

Herein, we present the design and development of a 'Non-uniform Rational B-spline (NURBS)' based iso-geometric approach for the analysis of a number of 'Boundary Value Problems (BVPs)' relevant in hydrodynamics. We propose a '*Potential Function*' based 'Boundary Element Method (BEM)' and show that it holds the advantage of being computationally efficient over the other known numerical methods for a wide range of external flow problems. The use of NURBS is consistent, as inspired by the 'iso-geometric analysis', from geometric formulation for the body surface to the potential function representation to interpolation. The control parameters of NURBS are utilised and they have been explored to arrive at some preferable values and parameters for parameterization and the knot vector selection. Also, the present paper investigates the variational strength panel method, and its computational performance is analyzed in comparison with the constant strength panel method. The two variations have been considered, e.g. linear and quadratic. Finally, to illustrate the effectiveness and efficiency of the proposed NURBS based iso-geometric approach for the analysis of boundary value problems, five different problems (i.e. flow over a sphere, effect of the knot vector selection on analysis, flow over a rectangular wing section of NACA 0012 aerofoil section, performance of DTMB 4119 propeller (un-skewed), performance of DTNSDRC 4382 propeller (skewed)) are considered. The results show that in the absence of predominant viscous effects, a '*Potential Function*' based BEM with NURBS representation performs well with very good computational efficiency and with less complexity as compared to the results available from the existing approaches and commercial software programs, i.e. low maximum errors close to 1×10^{-3}, faster convergence with even up to 75 % reduction in the number of panels and improvements in the computational efficiency up to 32.5 % even with low number of panels.

NOMENCLATURE

2D	Two dimensional,
3D	Three dimensional,
BEM	Boundary element method,
CAD	Computer aided design,
CAGD	Computer aided geometric design,
CFD	Computational fluid dynamics,
DTMB	David Taylor model basin,
FEA	Finite element analysis,
FEM	Finite element method,
FVM	Finite volume method,
IGA	Iso-geometric approach,
NACA	National advisory committee for aeronautics,
NURBS	Non-uniform rational B-spline,
V	Volume of the closed 3D domain,
S	Boundary of the closed 3D domain,
$\vec{n}$	Unit normal vector,
S_B	Body surface,
S_w	Wake surface,
S_H	Hub surface,
S_∞	Outer control surface of an arbitrary domain
ϕ	Potential function,
Γ	Circulation around the body,
$\bar{x}$	Field point in 3D,
$\bar{x}_0$	Singular or pole point in 3D,
δ	Dirac's delta function,
$G(\bar{x},\bar{x}_0)$	Green's function,
r	Distance of the field point from the singular point,
$\bar{r}$	Radial vector,
$\vec{U}_\infty$	Inflow free stream velocity,
$h(u)$	Curve data point,
H_i	Control points of the NURBS curve,
$Rc_{i,p}(u)$	Rational basis functions,
$R_{i,l}$	NURBS surface control points after interpolating in the u direction,
S_N	Patch number,
N^ϕ	Number of data points in the u parametric direction for potential function,
M^ϕ	Number of data points in the v parametric direction for potential function,
$N_{i,p}(u)$	B-spline basis-functions of the degree p in u parametric direction,
$N_{j,q}(v)$	B-spline basis-functions of the degree q in v parametric direction
p	Degree of surface in the u parametric direction,

q Degree of surface in the v parametric direction,
$w_{i,j}$ Weights associated with a control point of the NURBS surface,
a Coefficient of centripetal parameterization,
K Number of symmetry,
$\theta_s(r)$ Distribution of the skew angle,
$x_s(r)$ Distribution of the rake angle,
$c(r)$ Distribution of the chord length,
$\Phi(r)$ Distribution of the pitch angle,
$f(r)$ Distribution of the camber,
$t(r)$ Distribution of the thickness,
R_h Radius of the hub,
X_u Computational axial distance in the upstream region of the propeller,
X_d Axial distance from the trailing edge of the blade to the beginning of the fairwater,
X_t Axial length of the fairwater,
D Diameter of the propeller,
R Radius of the propeller,
X_b Axial distance between the leading and trailing edges,
X_u^T Distance from the origin to the upstream end,
X_d^T Distance from the origin to the downstream end,
$\varphi_{i,j}^{u,v}$ Unknown potential function control vertices,
$\vec{U}_A$ Mean advance velocity of the propeller,
$\vec{\Omega}$ Rotational speed of the propeller
dS Differential surface element,
J_c Jacobian,
N_g Order of Gauss-Legendre product rule,
d Representative length-wise scale of the surface,
L Distance of the centroid of surface from the field point,
χ Sub-division criteria to be satisfied,
C_p Pressure coefficient,
P_∞ Pressure at the free stream,
P Static pressure,
U Perturbation velocity,
U_T Total perturbation velocity,
$U_{induced}$ Induced velocity,
Δt_i Time step,
K_T Thrust coefficient,
K_Q Torque coefficient,
Q Torque,
T Thrust,
J Advance ratio,
ρ Density of the fluid,
A_i Area of the i-th panel,
n Number of the propeller revolution per sec,
θ Azimuth angle,
U_{surf} Velocity at the surface of ellipsoid,
$U_{\max}$ Maximum velocity at the surface of ellipsoid,
AX Semi lengths of axis of ellipsoid in the x direction,
BY Semi lengths of axis of ellipsoid in the y direction, and
CZ Semi lengths of axis of ellipsoid in the z direction.

1. INTRODUCTION

Interestingly, the naval architecture community has been one of first users of the computers and computational methods for the design, analysis and production of ships. In modern integrated environment, it is possible to use computer aided design (CAD) to explore design options and subsequently employ computational methods with the CAD model for design and development. The CAD model needs a mathematical geometric definition for any object that needs to be analyzed, e.g. for structural analysis using the finite element analysis and for hydrodynamic analysis using the computational fluid dynamic analysis etc. At present for the geometric definition, most of the existing CAD systems rely upon 'Non Uniform Rational Basis Spline (NURBS)' and NURBS is considered a 'de-facto' standard in modern CAD systems. Although, there are problems associated with the NURBS (e.g. restricted for use only to rectangular topology, and impossible representation of the intersection of two NURBS surfaces by a trimmed NURBS surface without introducing gaps in the model, etc.), still the NURBS offers great flexibility and precision for handling both analytic (surfaces defined by common mathematical formulas) and free form shapes, for more details see Piegl & Tiller (1996), Farin (1999).

Recently, Hughes *et al.* (2005) and Cottrell *et al.* (2009) introduced an iso-geometric approach, wherein the definition or the approximation of the geometry and the field variable was done using the NURBS defined over the identical parametric space. The iso-geometric approach provides the consistent representation for the geometry and the solution approximation, thus results in a more accurate numerical solution. From the numerical analysis perspective, it is well known that the Boundary Element Methods (BEMs), are computationally efficient for the external flow problems where the volume to surface area ratio is low, and the reason being that in the case of the boundary element method the dimension of the discretization reduces by one as compared to the case of three-dimensional problems. This results into computational savings. This advantage of the BEM has motivated researchers to investigate panel methods for the external flow problems, for more details see Hess & Smith (1964), Lee (1988).

Once the geometric definition is ready with a CAD model, it needs to be analyzed. It is obvious that a

consistent use of geometric definition from CAD to FEA to CFD to manufacturing simulation will help in reducing the design and analysis time, and will integrate the design and analysis process. This idea of integration of CAD with FEA, CFD and manufacturing simulation has motivated researchers to develop a computational approach that offers the possibility of integrating finite element analysis (FEA) into conventional NURBS-based CAD design tools. And, this approach is called 'Iso-geometric Analysis', and was initiated by Cottrell *et al.* (2009) and Hughes *et al.* (2005). Before the initiation of the iso-geometric analysis, it was required to convert data between and across the CAD, FEA and CFD software packages to analyze new designs during development, and this conversion is difficult because the computational geometric approaches are different for CAD, CFD and FEA. This paper is inspired by the same 'iso-geometric analysis' approach of Cottrell *et al.* (2009).

The basic aim of any numerical method is to achieve the higher accuracy with less computational cost, i.e. computational time, computational effort, and memory required. Accuracy in the numerical method can be increased by reducing the domain error, i.e. error arising due to the limitation of the meshing elements to exactly represent the body surface or volume) and the truncation error. The truncation error can be minimized using either more number of points in the power series expansion or by using higher order approximations for the field variables or by doing both. Most of the meshing tools in the industry are capable of generating mesh using (triangular, hexagonal, or quadrilateral etc.) various types of elements, and they all will have straight edges (C^0 continuity). Most of the complex engineering geometries are composed of either conic shapes or free form shapes and this demands the need for heavy mesh generation (i.e. more number of mesh elements) which results in high computational cost (computational time and memory required). Nevertheless, if one uses the mesh elements having curved edges (i.e. at least C^1/ G^1 continuous) instead of straight edges, one can exactly represent the surface or the volume of the body with small number of mesh elements. Hence, the computational cost will reduce by a significant amount and lead to more accurate results due to reduced domain or discretization error. From the CAD background, it is known that the NURBS can represent conical shapes exactly without any discretization error, and they are better suited for the representation of the free form shapes, for detail see Piegl & Tiller (1996), Farin (1999).

In the present paper we focus on a class of engineering hydrodynamic problems in which fluid flow past the bodies can be studied by Laplace's equation, e.g. subsonic flow around wings, flow around spheres, ellipsoids, and flow past marine propellers. An exact solution for the flow past three-dimensional bodies exists only for some simple primitive geometric bodies. Therefore, numerical techniques are required to analyze the more general 3D curved free-form shaped bodies. Some of the generally used numerical techniques for the flow past the 3D curved free form bodies are: finite difference method, finite element method, finite volume method, and boundary element method (boundary integral equation). When it comes to computational cost in the case of external flow problems, the boundary element method holds the edge over the other numerical methods, because in case of the boundary element method, the dimension of discretization reduces by one as in case of three dimensional problems, and one has to discretize only the surface of body, for more detailed description see Becker (1992).

The remaining of this paper is organized: Section 2 briefly reviews the existing literature and mentions our basic motivation, Section 3 discusses the details about the mathematical background for the problem, Section 4 presents the details about the mathematical background for the NURBS, Section 5 describes the numerical formulation of the problem, Section 6 presents various numerical examples and discussions, and Section 7 presents the summary, conclusions the scope of future work. A more detailed treatment of the results of this paper can be found in a recent thesis by the first author (Goel (2016)).

2. REVIEW OF LITERATURE AND BASIC MOTIVATION

In the available literature large numbers of different panel methods have been developed for a variety of applications, leading to different types of applications for the analysis of steady performance of the marine propellers. Most of the initial papers were based on the velocity function based formulations in which the boundary condition on the body surface is satisfied through the direct computation of the velocity. It is well known that the velocity function is singular by one order higher as compared to the potential function and this causes numerical un-stability. Based upon this, the proposed paper uses a potential function based panel method formulation that is more suitable for numerical computation. There exists a wide range of theories for the prediction of flow around the propellers. For predicting the flow field parameters around the propellers, the panel methods have been widely accepted as a useful tool for the aerodynamic and hydrodynamic design of propellers, e.g. Koyama *et al.* (1986), and Lee (1988).

In one of the earliest works, Hess & Smith (1964) studied a constant strength panel method to calculate the incompressible potential flow around arbitrary, non-lifting three-dimensional bodies. Later, Hess (1972) applied the same formulation as of Hess & Smith (1964) for the flow around lifting three-dimensional bodies. In both of these methods body surface was approximated by planar triangular or quadrilateral panels that are known to have only lower degree of continuity, e.g. C^0 continuity.

In the case of non-lifting bodies, the surface of the body was approximated by unknown source singularity. In the case of lifting surface bodies, the surface of the body was approximated by source singularity (i.e. to consider thickness of the body) and unknown strength of doublet or vortices singularities to account for the lifting aspect of the flow. The basic advantage of the constant strength panel method is its simplicity and less complexity involved in the computation. Morino & Kuo (1974) introduced a panel method based on Green's formula in which primary unknown is the potential function. Prior to Morino & Kuo (1974) all the methods were mainly based on velocity function based formulation Morino & Kuo (1974) introduced potential function based formulation which is more stable than the velocity function based numerical formulation. This potential function based formulation is more stable than the velocity function based numerical formulation. The other main contribution of Morino & Kuo (1974) formulation was the imposition of Kutta condition at the trailing edge of the lifting bodies.

Hess & Velarezo (1985) applied the lower order surface panel method for the analysis of steady performance of the marine propeller. From Hess & Velarezo (1985) it can be concluded that surface panel method suffers when the thickness of the propeller blade becomes very small, e.g. towards the tip of the propeller. Koyama *et al.* (1986) applied the lower order panel method for the analysis of the marine propeller. It was found that the pressure distribution near the tip of the blade predicted by Koyama *et al.* (1986) also was not accurate. It was mainly because the Kutta condition applied by Koyama *et al.* (1986) was not able to account for the cross flow effects of the three-dimensional flow. Lee (1988) proposed a potential function based panel method for the analysis of marine propellers in steady flow. Prior to his work lifting surface theory was used for the design and analysis of marine propellers. Furthermore, before Lee (1988) the hub surface effect was not included in any of the lifting surface based formulations that compute a pressure distribution, which is not valid in the real world marine propellers. To rectify all of these difficulties associated with the lifting surface theories, Lee (1988) proposed a panel method for the hydrodynamics analysis of the propeller including the propeller hub to account for the three-dimensional cross flow effect at the trailing edge, a pressure Kutta condition is applied. The pressure Kutta condition requires that the pressure on the last panels at the trailing edge be equal. Due to the non-linear aspect of the pressure Kutta condition, an iterative procedure was employed. Lee (1988) observed that potential function based methods are more accurate for thin sections as compared to the velocity function based methods. The main drawback of the constant panel method is that it requires a large number of panels to obtain the accurate results. Other main drawback of the constant strength panel method is the lower order continuity of the solution. The basic advantage of the constant strength panel method is its simplicity and less complexity involved in the computation. In order to achieve the same level of accuracy as of constant strength panel method using only a small number of panels, higher order panel methods have been proposed in the past. Higher order panel methods provide the higher order accuracy to the field variables (potential function). Different higher order approaches have been proposed in the past for different types of the boundary value problems.

Possibly, the first, Roberts & Rundle (1973) proposed a higher order panel method, and they used a paraboloid panel surface to model the body surface. In their method quadratic source and doublet strength had been used with no penetration boundary condition. This method was computationally very expensive as compared to the constant panel method. A different higher order approach was developed by Johnson & Rubbert (1975) and they proposed a higher order panel method wherein the body surface is approximated by the paraboloid panels. In their method a linearly varying source distribution and quadratically varying dipole distribution over each panel was proposed in the tangent plane variables. Hess (1979) also used the same approach as of Johnson & Rubbert (1975) and the author introduced a higher order panel method where he used cubic panel shape with quadratic density of the source. His approach leads to an extremely complicated algorithm. He concluded that the higher order panel method scheme is superior to the constant strength panel method for interior flows, e.g. flow through duct of varying cross section. Atkinson (1990) studied higher order approach, where the body surface was discretized by curvilinear triangular panels. Xu (1992) applied an approach identical to Atkinson (1990), and he used curvilinear rectangular panels instead of curvilinear triangular panels used by Atkinson (1990). The unknown potential over each panel was approximated using the same basis set as used for the description of panel. The approaches of Atkinson (1990) and Xu (1992) provide overall better accuracy when compared to the constant strength panel method.

Higher order methods using the Lagrangian interpolation function suffer mainly due to the discontinuous spatial derivatives of the potential across the panel boundaries. Hsin *et al.* (1993) investigated the idea of using the B-spline representation for the geometric and the potential function representation. Using the B-spline for geometry and the potential function representation provides several degree of continuity to both the potential function and its derivative. Their results showed that it was not only accurate, but also robust and efficient. Maniar (1995) proposed a B-spline based three-dimensional higher order panel method to study the motion of the bodies in an infinite field, and the motion of the bodies in the presence of the free surface. In his work, the potential function and the geometry of the body are allowed to have any degree of continuity. The author successfully applied the method for the zero-speed frequency-domain radiation and diffraction problems and found that higher

order panel method is computationally efficient and capable of obtaining accurate point wise values for the potential function. From his work, it can be concluded that B-spline based panel method not only provides good accuracy and efficiency in terms of computational cost but are also capable of solving a variety of problems, some of which can be difficult or impossible to solve with constant strength panel methods.

Lee *et al.* (1998) and Danmeier (1999) presented a geometry independent higher order method in which the geometrical and hydrodynamic representations are decoupled. In their works, the potential function was represented by a set of B-spline basis functions, but the geometry can be modeled by any regular parameterization. Kim & Nam (1999) proposed a B-spline panel method where surface was described by the NURBS which provides more accurate geometric representation for the conic surfaces and are better suited to model free form surfaces. Lee & Kerwin (2003) introduced a B-spline higher order panel method and applied it to the two dimensional lifting problems. They used the approach identical to Hsin *et al.* (1993) wherein the two dimensional body profile and the potential function both are represented using B-spline. Kim et al. (2007) used the approach identical to Hsin *et al.* (1993), and proposed a B-spline based higher order panel method for the analysis of steady flow around marine propellers. The authors applied a null pressure jump Kutta condition at the trailing edge, which was found to be effective in stabilizing the solution process and in predicting the correct solution. The authors concluded that the B-spline based high-order panel method is robust, can handle the thin trailing edge and the tip region flow. Smaller number of panels can be used for the practical purpose without sacrificing the accuracy.

2.1. RESEARCH CONTRIBUTION

From the literature review, we observe the following critical points that have motivated our work:

- Higher order panel method is an effective method of the potential flow analysis and there has been a considerable interest in developing a numerical solution schemes for a variety of the potential flow problems.

Our motivations and research contributions are:

- Because the higher order panel method is known to be efficient, we aim for the development of a higher order panel method.
- Since, an 'iso-geometric' approach (IGA) provides the consistent representation for geometry and solution approximation and therefore we adopt the consistent use of NURBS for all the representations.
- We build upon the previous works of Farin (1999) and Piegl and Tiller (1996) to use the basic mathematics of NURBS and Kim *et al.* (2007) to use the same hydrodynamic modeling of propeller. These works are foundational in nature and hence these are referred. Our model extends the previous works to include real NURBS with weights and formulation is capable of handling different applications related to fluid flow over complex geometries, e.g. fluid flow over a sphere; fluid flow over a rectangular wing section of a NACA 0012 aerofoil; steady state performance of an un-skewed propeller (DTMB 4119 propeller); and a skewed propeller (DTNSRDC 4382 propeller). Additionally, we explore the use of NURBS in full generality, e.g. use of different schemes of knot vector selection.
- Herein, we analyse the performance of IGA through detailed comparative studies with results from 'Constant Source Panel Method (CSPM)', 'Higher Order Panel Method (HOPM)' and 'Finite Volume Method (FVM)'.

3. MATHEMATICAL BACKGROUND

To formulate the problem, a closed three-dimensional domain V with the boundary S, the unit normal vector $\vec{n}$ and the orientation of $\vec{n}$ to S as shown in Figure 1, is considered. Here boundary S is composed of the body surface S_B, the wake surface S_w, and the outer control surface S_∞ surrounding the body and the wake surface. The body is subjected to the inflow velocity $\vec{U}_\infty$. We make certain assumptions: Fluid is incompressible, fluid is inviscid and fluid flow is irrotational. The following boundary conditions are satisfied:

- The kinematic boundary condition is satisfied on the solid body surface S_B, i.e.

$$\frac{\partial \phi}{\partial n} = -\vec{U}_\infty . \vec{n}. \tag{1}$$

- The wake surface is assumed to have a zero thickness. The normal velocity jump and the pressure jump across S_w are zero, while a jump in the potential is allowed, i.e.

$$\left(\Delta p\right)_{on\ S_W} = p^+ - p^- = 0, \text{ and} \tag{2}$$

$$\left(\Delta \frac{\partial \phi}{\partial x}\right)_{on\, S_w} = \left(\frac{\partial \phi}{\partial n}\right)^+ - \left(\frac{\partial \phi}{\partial n}\right)^- = 0. \tag{3}$$

For the steady lifting problem, the potential jump across the wake surface is the same as the circulation around the body, and is constant in the stream-wise direction on S_w, i.e.

$$\left(\Delta \phi\right)_{on\ S_w} = \phi^+ - \phi^- = \Gamma. \tag{4}$$

- A Kutta condition is required at the trailing edge to uniquely specify the circulation in case of the lifting flow problems, like flow around the wing section of a

NACA 0012 aerofoil or a marine propeller. In most general form, Kutta condition states that the flow velocity at the trailing edge (T.E.) remains bounded, i.e.

$$\left|\nabla\phi\right|_{T.E.} < \infty. \tag{5}$$

- On the control surface S, the perturbation velocity due to the body should vanish in the limit where this surface is an infinite distance from the body. This results into:

$$\nabla\phi \to 0, \text{ as } S_\infty \to \infty. \tag{6}$$

Now, with the above mentioned assumptions there exists a perturbation potential function ϕ, which satisfies the Laplace's equation:

$$\nabla^2\phi = 0. \tag{7}$$

Using the Green's identities, Equation (7) is reduced to (for detail see Danmeier (1999)):

$$\nabla.\left(\phi\nabla f - f\nabla\phi\right) = 0. \tag{8}$$

The Green's functions constitute a special class of harmonic functions that are singular at an arbitrary point $\bar{x}_0 = (x_0, y_0, z_0)$. By definition, a Green's function of Laplace's equation in three dimensions satisfies the singularity forced Laplace's equation:

$$\nabla^2 G\left(\bar{x},\bar{x}_0\right) + \delta\left(\bar{x}-\bar{x}_0\right) = 0, \tag{9}$$

where $\bar{x}$ is the field point in 3D, $\bar{x}_0$ is the singular or pole point in 3D, and δ is the Dirac's delta function in 3D. In the present paper, we select free space Green's function because it corresponds to an infinite solution domain in the absence of interior boundaries, and it is (for details see Cumming *et al.* (1972)):

$$G\left(\bar{x},\bar{x}_0\right) = \frac{1}{4\pi r}, \tag{10}$$

where $r = \left|\bar{x}-\bar{x}_0\right|$ is the distance of field point from the singular point. Applying Green's second identity Equation (8) for a non-singular function ϕ and a Green's function $G\left(\bar{x},\bar{x}_0\right)$ and using Equation (9), we obtain:

$$\phi\left(\bar{x}\right)\delta\left(\bar{x}-\bar{x}_0\right) = \nabla.\begin{bmatrix} G\left(\bar{x},\bar{x}_0\right)\nabla\phi(\bar{x}) \\ -\phi(\bar{x})\nabla G\left(\bar{x},\bar{x}_0\right)\end{bmatrix}. \tag{11}$$

Now, we apply Equation (11) to the control volume V that is the collection of closed surfaces denoted by the S, as shown in Figure 1. When the pole $\bar{x}_0$ is placed inside V, the left hand side of above equation is singular at the point $\bar{x}_0$. Using the distinctive properties of the delta function in 3D to perform the integration, and using the divergence theorem we obtain:

$$\begin{aligned}\phi\left(\bar{x}\right) = &-\iint_S G\left(\bar{x},\bar{x}_0\right)\left[\vec{n}.\nabla\phi\left(\bar{x}\right)\right]dS\left(\bar{x}\right) \\ &+\iint_S \phi\left(\bar{x}\right)\left[\vec{n}.\nabla G\left(\bar{x},\bar{x}_0\right)\right]dS\left(\bar{x}\right).\end{aligned} \tag{12}$$

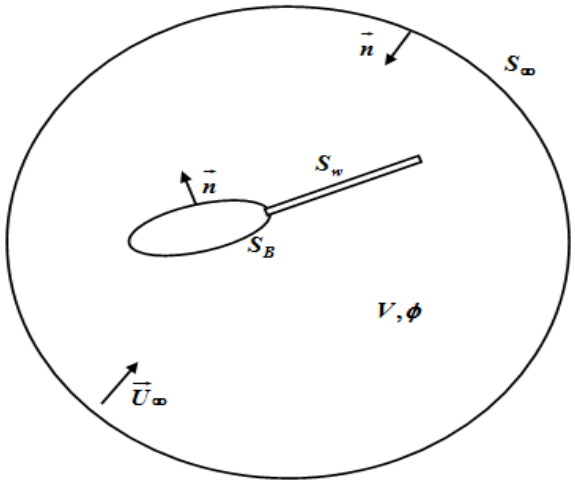

Figure 1: Basic convention of the arbitrary domain

As surface S is composed of the body surface S_B (propeller blade), S_H (hub surface) and the wake surface S_w, following following Lee (1988) and Lee (1989), we re-write Equation (12):

$$\begin{aligned}\frac{\phi\left(\bar{x}\right)}{2} = &\iint_{S_B\cup S_H}\left\{\begin{matrix}\left(-\phi\left(\bar{x}\right)\right)\dfrac{\partial G\left(\bar{x},\bar{x}_0\right)}{\partial n} \\ +\dfrac{\partial\phi\left(\bar{x}\right)}{\partial n}G\left(\bar{x},\bar{x}_0\right)\end{matrix}\right\}dS \\ &+\iint_{S_w}\left(-\Delta\phi\left(\bar{x}\right)\right)\frac{\partial G\left(\bar{x},\bar{x}_0\right)}{\partial n}dS\end{aligned} \tag{13}$$

where $G\left(\bar{x},\bar{x}_0\right) = \dfrac{1}{4\pi r}$ and here ϕ is the perturbation potential and $\vec{n}$ is the unit vector normal to the body and wake surfaces. Here the surface integral on S_B is defined to exclude the immediate vicinity of the singular point. As $\partial\phi\left(\bar{x}\right)/\partial n$ is known on the S_B from the kinematic boundary condition (Equation 1), therefore, Equation (13) is a Fredholm integral equation (Pozrikidis (2010)) of the second kind for the unknown dipole

strength ϕ, which is also the potential function over the body surface S_B.

Potential jump across the wake surface is equal to the difference between the potential values of the upper and lower surface at the trailing edge, which is Kutta condition. Discretization of Equation (13) leads to the linear system of equation for the unknown dipole strength ϕ. The surface velocity and the pressure distribution on the body surface S_B and S_H can be computed by the numerical differentiation of the potential distribution over these surfaces. This method is known as Morino's method as he was the first to introduce this method, for details see Morino & Kuo (1974).

4. BASIC MATHEMATICS OF NURBS

Following Cottrell *et al.* (2009), a NURBS entity in R^d is obtained by the projective transformation of a B-spline entity in R^{d+1}. In particular, conic sections, such as circles and ellipse, can be exactly represented by the projective transformations of the piecewise quadratic curves. Now, following Piegl & Tiller (1996), a p^{th} degree NURBS curve is defined:

$$h(u)=\frac{\sum_{i=0}^{n} N_{i,p}(u)\,w_i\,H_i}{\sum_{i=0}^{n} N_{i,p}(u)\,w_i}, \tag{14}$$

where H_i are the control points (forming a control polygon), w_i are the weights associated with these control points and $N_{i,p}(u)$ are the p^{th} degree B-spline basis functions defined on the non-uniform knot vector, i.e.,

$$u=\left[\underbrace{e,\ldots,e}_{p+1},u_{p+1},u_{p+2},\ldots,u_{m-p-1},\underbrace{f,\ldots,f}_{p+1}\right]. \tag{15}$$

In the present paper, it is assumed that $e=0, f=1$, and $w_i>0$. This assumption leads to unit interval parameterization and it is without any loss of generality. In Equation (14), B-spline basis functions are defined as:

$$N_{i,0}(u)=\begin{cases}1, & u_i\le u\le u_{i+1}\\ 0, & otherwise\end{cases}, \text{ and}$$

$$N_{i,p}(u)=\frac{u-u_i}{u_{i+p}-u_i}N_{i,p-1}(u) + \frac{u_{i+p+1}-u}{u_{i+p+1}-u_{i+1}}N_{i+p,p-1}(u). \tag{16}$$

Now, we define the rational basis functions:

$$Rc_{i,p}(u)=\frac{N_{i,p}(u)w_i}{\sum_{j=0}^{n} N_{j,p}(u)w_j}. \tag{17}$$

Herein, we use the global surface interpolation method to calculate the control points of the surface from given data points. For more details about the NURBS and global surface interpolation see Piegl and Tiller (1996).

4.1 EFFECT OF WEIGHTS ON THE NURBS REPRESENTATION

The NURBS provides an additional control parameter that is the weight associated with control point of the control polygon. This extra control feature of the NURBS provides them an additional advantage over the B-spline and other polynomials. As we know if $w_i=1$ for all i or all the weights are equal then, NURBS basis functions reduce to the B-spline basis functions. The effect of weights on NURBS representation of the curve is shown in Figure 2a. To show the effect of weights on NURBS curve, we consider the arbitrary data points in the space as shown in the Figure 2a. At first, we perform the global interpolation to compute unknown control points of the control polygon, i.e. through global interpolation Piegl & Tiller (1996). After computing the control points, we vary the weights associated with control points to study the effect of weights on the curve approximation. Figure 2a shows a problem of curve approximation by varying the weight of a control point from 0.0 to 1.0, i.e. weight W6 in the present example. We observe from Figure 2a that the weights have the pulling effect on the curve approximation. As one keeps on increasing the weight associated with any of the control point, curve will have a tendency of getting pulled towards that control point. As one keeps on decreasing the weight associated with the control point, curve will have the tendency to move away from the control point. As shown in Figure 2a, when the value of weight associated with the sixth control point reduces to zero, it does not have any effect on the representation of the curve. In this way, weights associated with the control points play a vital role in the curve, surface or volume representation of the object as the basis curve representation is followed in surface and volume too. We note here that as the optimisation of the weights in the NURBS representation is fairly an open problem, no automatic computation of the weights is possible. The weights are easy to be assigned a specific value rather than computing them through optimisation. We assign different combinations of the weights specific to the problem and report them in our results.

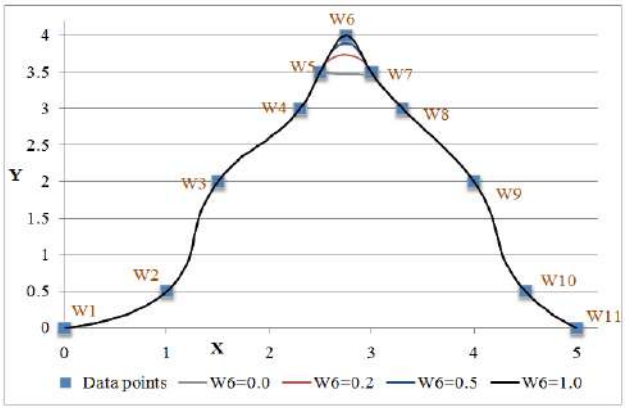

(a) Effect of the weights on NURBS representation of the curve.

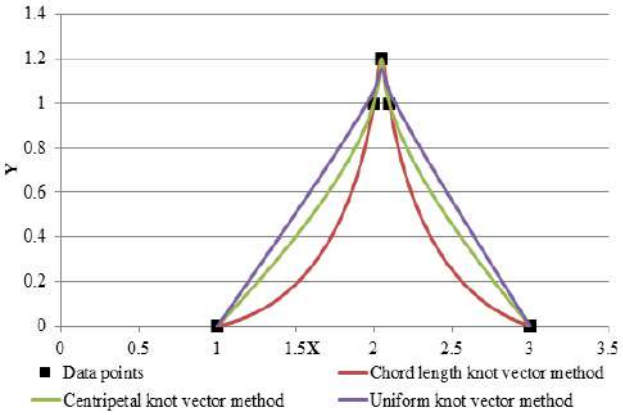

(b) Effect of the knot vector selection on NURBS representation of the curve.

Figure 2: Effect of the weights and knot vector selection on NURBS representation of the curve.

4.2 EFFECT OF THE KNOT VECTOR SELECTION ON CURVE REPRESENTATION

We assume that the parameter lies in the range of $u \in [0,1]$, and $v \in [0,1]$. To study the effect of different types of knot vectors, we consider a set of arbitrary data points as shown in Figure 2b. In Figure 2b, the curves are approximated using different methods of knot vectors selection, i.e. uniform knot vector, chord length knot vector or centripetal knot vector for $u \in [0,1]$. We observe from Figure 2b that the centripetal knot vector method provides a tighter fit to the curve for the given data points, and is very much suited for the representation of the most of the complex engineering shapes especially when the data points have sharp bends, e.g. propeller data or unequally spaced data points. As the centripetal knot vector method provides a tighter approximation for the curve or the body surface, we investigate this in our work. Also, the effect of the coefficient of centripetal parametrization - a - on the analysis and body representation is studied.

5. NUMERICAL FORMULATION OF THE PROPOSED PROBLEM

A discretized form of Equation (13) can be applied to any arbitrary general body in the potential flow. Herein, a panel is the mesh that composes of NURBS patches to represent the body and wake surfaces, and in both of them the degree can be varied to any desired degree. In constant strength panel method, the singularity strength distribution on the meshes is assumed to be piecewise constant over the meshes.

In case of the higher order panel method, the singularity strength distribution can be varied from linear to quadratic to cubic over the panels of the body and wake surfaces. The collocation approach is adopted for the analysis. In case of the constant strength mesh method the discretized integral equation is satisfied at the centroid of each of the meshes and in the higher order formulation, discretized integral equation is satisfied at the four collocation points to generate enough number of equations for the unknown dipole strength.

From the solution of the linear system of equations, any of the desired flow quantities of physical interest can be computed.

5.1 ISO-GEOMETRIC FORMULATION (IGF)

The important idea of IGF is that the geometric definition is consistent from geometry to analysis, i.e. body to analysis of the fluid flow. In our IGF of the present paper, we focus on: IGF 1 - Surface geometric formulation and IGF 2 - NURBS representation of the function for potential flow solution.

5.1 (a) IGF 1 - Surface geometric formulation

In the surface geometric formulation, we define: 1) Surface description, 2) blade geometry and 3) Hub geometry. The individual details are:

- *Surface description:* The body and wake surfaces, over which the integral equation is to be solved, are described by the N patches, i.e.,

$$S = S_1 + S_2 + S_3 + S_4 + \ \ldots \ + S_N. \qquad (18)$$

Following, Piegl & Tiller (1996), each of the patches (e.g. S_i) is described parametrically by a NURBS patch, i.e.,

$$x(u_k, v_l) = \frac{\sum_{i=1}^{N^\phi} \sum_{j=1}^{M^\phi} X_{i,j} N_{i,p}(u) N_{j,q}(v) w_{i,j}}{\sum_{i=1}^{N^\phi} \sum_{j=1}^{M^\phi} N_{i,p}(u) N_{j,q}(v) w_{i,j}}, \qquad (19)$$

where N^{ϕ} and M^{ϕ} are the number of data points in the u and v parametric directions respectively, $N_{i,p}(u)$ and $N_{j,q}(v)$ are the B-spline basis-functions of the degree p and q in the parametric variables u and v respectively and $x(u_k, v_l)$ are the data points describing the body and wake surfaces. Here $w_{i,j}$ are the weights associated with the control points on the surfaces and $X_{i,j}$ are the control points representing the body surface. These control points are computed using a global interpolation. Figure 3a shows an example of a smooth three-dimensional surface, composed of number of patches each of which is described by a NURBS patch in the form of Equation (19). The rectangular parametric space, which is mapped by Equation (19) onto the physical surface, is:

$$[u_e, u_{e+p}) \; x \; [v_f, v_{f+p}), \tag{20}$$

where u_e and v_f are the e^{th} and f^{th} knots of the knot vectors *u* and *v* respectively. The vector space given in Equation (20) is referred as the usable parametric space. The geometric control points are computed using the global interpolation technique as explained before. Figures 3b, 3c and 3d show the technical details of NURBS representation of cubic surface patch.

- *Blade geometry:* The propeller blade consists of K identical blades and an axi-symmetric hub. For the steady flow problem, both the geometry and the singularity distribution are repeated identically on each blade and on each of the inter blade segments of the hub. In order to take the advantage of the rotational symmetry of the propeller system, only $(1/K)^{th}$ portion of the propeller, i.e., only one blade and the $(1/K)^{th}$ portion of the hub is discretized. Effect of the remaining portions of the propeller is included in the computation of the influence functions. We report analysis for two propellers: Un-skewed propeller (DTMB 4119 propeller), and skewed propeller (DTNSRDC 4382). The geometric properties of propellers are listed in Table 1 (DTMB 4119 propeller) and Table 8 (DTNSRDC 4382).

- *Hub geometry:* The geometry of the hub is defined by any of the profile curves, which can be anything from a constant diameter cylinder to a complete axisymmetric body on which the propeller in mounted. A realistic geometry is a semi-infinite ellipsoid on the upstream with a given fairwater geometry downstream of the blades.

The standard propeller coordinate system and notations adapted from Lee (1988) are shown in Figure 4a. The geometry of the hub that is used in the analysis is shown in Figure 5a. The geometry of hub can be determined by the following input parameters: Maximum hub radius R_h, Computational axial distance in the upstream region of the propeller X_u, Axial distance from the trailing edge of the blade to the beginning of the fairwater X_d and axial length of the fairwater X_t. The axial distance between the leading and the trailing edges, X_b in Figure 5a is determined from the geometry of the blade at the root section of the propeller blade. The $X_u{}^T$ and $X_d{}^T$ in Figure 5a, are the distances from the origin to the upstream to the downstream ends of hub. The arrangement of hub meshes is selected to minimize the possible discretization errors due to miss-match of the hub meshes and the blade or wake meshes. Over the axial location between leading and trailing edges, the hub meshes are arranged to match the blade meshes at intersection. The meshes on the hub are arranged to provide a finer spacing near the propeller blade section and coarser spacing upstream to reduce the computational cost. The axial coordinates of intermediate meshes between the blades needs to be adjusted in order to avoid the badly shaped meshes in this region, as this region is extremely important from the analysis point of view. If the axial coordinates of upstream meshes are required to be the same in circumferential direction, the meshes near leading edge will turn inside-out. A special care is to be taken to avoid this condition. The geometry definition and mesh distribution for the DTMB 4119 propeller in both the front and side-views are shown in Figures 4b and 5b.

5.1 (b) IGF 2 - NURBS representation of the function for potential flow solution

The potential function on each of the rectangular parametric patches is approximated as the NURBS function, i.e.

$$\phi(u_k, v_l) = \frac{\sum_{i=1}^{N}\sum_{j=1}^{M} \varphi_{i,j}^{u,v} \, N_{i,p}(u) M_{j,q}(v) w_{i,j}}{\sum_{i=1}^{N}\sum_{j=1}^{M} N_{i,p}(u) M_{j,q}(v) w_{i,j}}, \tag{21}$$

where $N_{i,p}(u)$ and $M_{j,q}(v)$ are the B-spline basis functions of the degree of p and q respectively, $\varphi_{i,j}^{u,v}$ are the unknown potential control vertices, and N and M are the numbers of potential control vertices in u and v directions respectively.

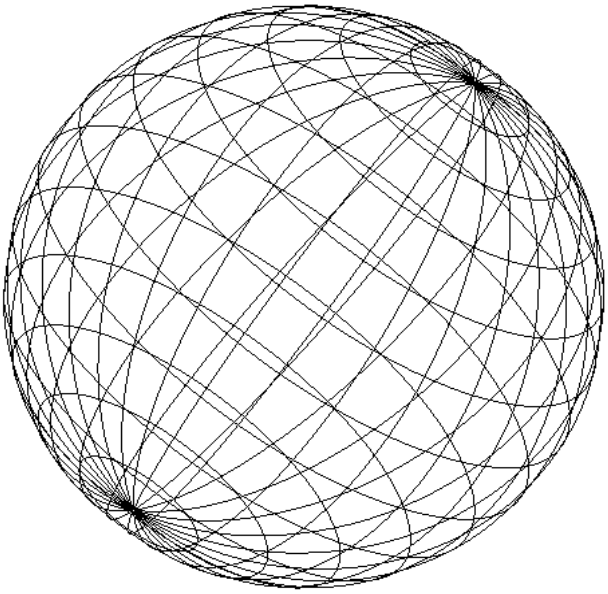

(a) Smooth representation of sphere surface.

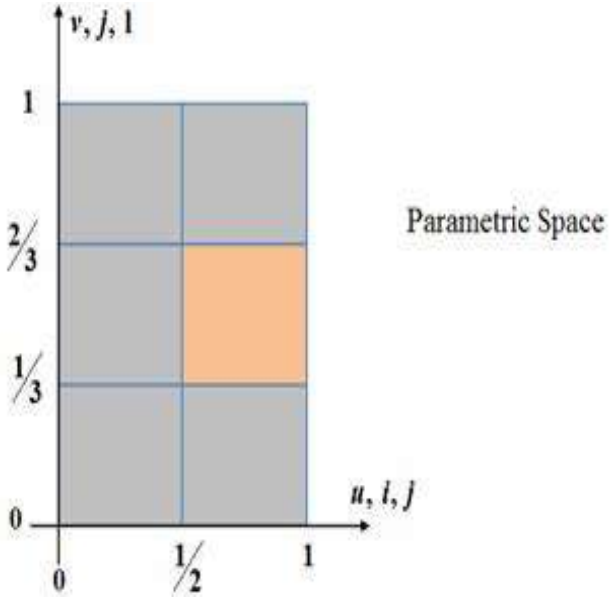

(b) Parametric space definition for the NURBS surface representation.

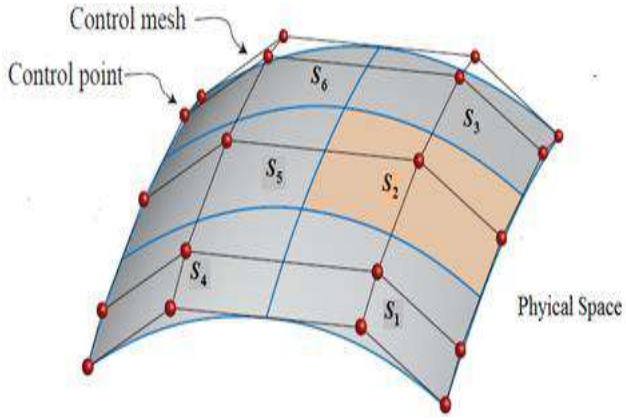

(c) Definition and description about the control mesh and points for the NURBS surface representation in physical and parametric spaces.

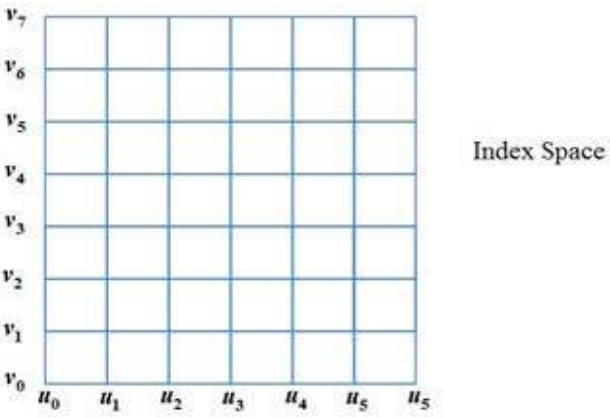

(d) Definition and description about the index spaces for the NURBS surface representation in parametric space.

Figure 3: Smooth representation of the sphere surface and the technical details of NURBS representation of surface patch.

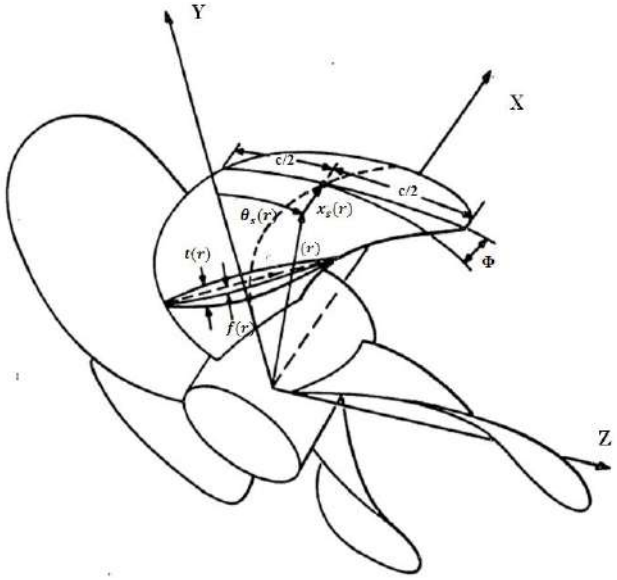

(a) Standard propeller coordinate system and the notations adapted from Lee (1988).

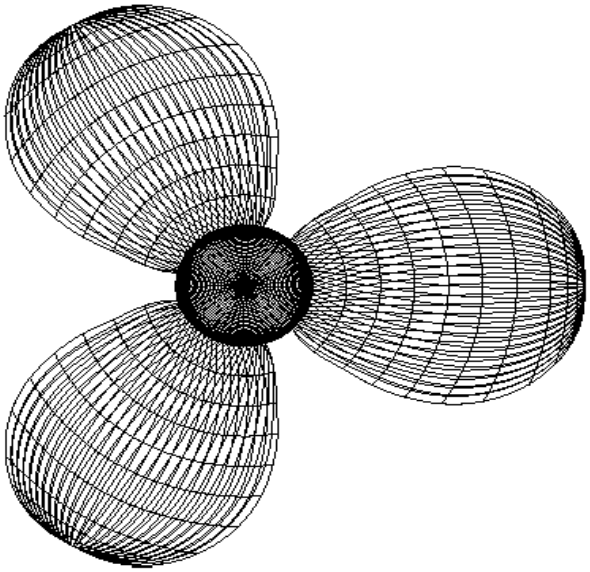

(b) Geometry definition and panel distribution for the DTMB 4119 propeller (front-view).

Figure 4: Standard propeller coordinate system and the notations adapted from Lee (1988), and the geometry definition and mesh distribution for the DTMB 4119 propeller (front-view).

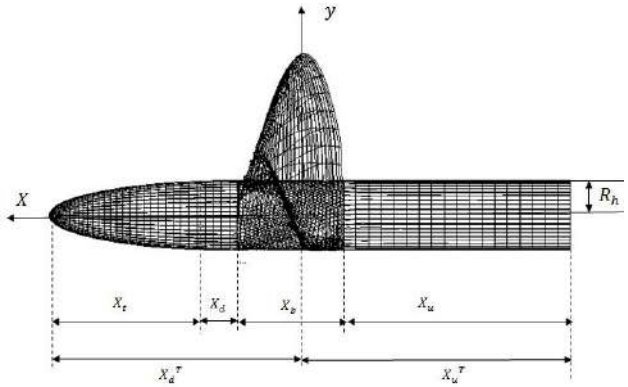

(a) Standard geometry notations of the propeller hub adapted from Lee [6].

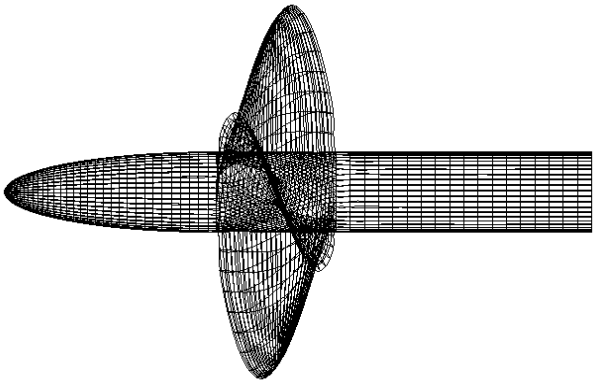

(b) Geometry definition and panel distribution for the DTMB 4119 propeller (side-view).

Figure 5: Standard geometry notations of the propeller hub adapted from Lee (1988) and the geometry definition and mesh distribution for the DTMB 4119 propeller (side-view).

The NURBS used for representing geometry and potential function need not to be necessarily the same, i.e. not necessarily iso-parametric. Possibly, they can differ in both the parameters, e.g. the degree of approximation and the knot vector they are based on. In the IGA a reasonable restriction on the NURBS representation of the both the geometry and potential function is that the usable parametric space for both the geometry and potential function should be identical. Herein, the same basis functions have been used to represent both the geometry and the potential functions. A patch is seen as a macro-element, regrouping several elements and representing an entire physical domain or a part of it. Many simple domains can be represented by only one patch. Instead of using sub-domains of the physical domain, patches play the role of sub-domains in IGA. Parametric space is local to patches and within each patch material models are assumed to be uniform. Knot vectors in the parametric space are then used to define the elements. This 'parametric space that is local to patches' is the usable parametric space. Hence, in the present paper, in case of the higher order mesh method, an 'iso-parametric' and 'iso-geometric' representation of the potential and the geometry is used.

5.1 (c) Discretization of integral equation using the NURBS representation of potential function

As discussed previously the integral equation for the analysis around the lifting body is:

$$\frac{\phi\left(\bar{x}\right)}{2} = \iint_{S_B \cup S_H} \left\{ \begin{array}{l} \left(-\phi\left(\bar{x}\right)\right) \dfrac{\partial G\left(\bar{x},\bar{x}_0\right)}{\partial n} \\ +\dfrac{\partial \phi\left(\bar{x}\right)}{\partial n} G\left(\bar{x},\bar{x}_0\right) \end{array} \right\} dS, \\ + \iint_{S_W} \left(-\Delta\phi\left(\bar{x}\right)\right) \frac{\partial G\left(\bar{x},\bar{x}_0\right)}{\partial n} dS \tag{22}$$

where $\phi\left(\bar{x}\right)$ is the perturbation potential, $\vec{n}$ is the unit normal vector to the body and wake surface and $G\left(\bar{x},\bar{x}_0\right)$ is the Green's function and it is defined:

$$G\left(\bar{x},\bar{x}_0\right) = \frac{-1}{4\pi r}, \tag{23}$$

with the kinematic boundary condition:

$$\frac{\partial \phi}{\partial n} = -\vec{U}_\infty . \vec{n}, \tag{24}$$

where $\vec{U}_\infty = \vec{U}_A$ in case of wing body and $\vec{U}_\infty = \vec{U}_A - \vec{\Omega} \times \vec{r}$ in case of the propeller, and $\vec{U}_\infty$ is the velocity circumferential mean on-coming stream past a fixed blade at radius r, and it is defined by circumferential mean advance velocity $\vec{U}_A$ and the rotational speed of the propeller $\vec{\Omega}$. The blade surface patch is discretized in to $(N^\phi - p, M^\phi - q)$ meshes using the usable parametric space (as defined previously in the beginning of Section 5.1 (b)) of the knot vectors as described previously in Equation (19).

The wake surface patch, which sheds downstream from the trailing edge, can be represented by a set of $M^\phi - q$ stream-wise strips with the constant normal dipole on each of the span-wise location. The discretization into a set of $(N^\phi - p, M^\phi - q)$ meshes on the blade and $M^\phi - q$ strips in the wake, yields to discretized form of Equation (11):

$$\frac{\phi\left(\bar{x}\right)}{2} = \sum_{c,d}^{N^\phi - p, M^\phi - q} \iint_{S_{c,d}} \left\{ \begin{array}{l} \left(-\phi\left(\bar{x}\right)\right) \dfrac{\partial G\left(\bar{x},\bar{x}_0\right)}{\partial n} \\ +\dfrac{\partial \phi\left(\bar{x}\right)}{\partial n} G\left(\bar{x},\bar{x}_0\right) \end{array} \right\} dS \\ + \sum_{d}^{M^\phi - q} \iint_{S_d{}^w} \left(-\Delta\phi\left(\bar{x}\right)\right) \frac{\partial G\left(\bar{x},\bar{x}_0\right)}{\partial n} dS. \tag{25}$$

From the definition of the NURBS basis functions, it is known that there are only $(p+1, q+1)$ non-zero basis functions at each of the knot span defined by the space between the adjacent knots, and now the potential function from Equation (21) is rewritten as a $(p+1, q+1)$ term summation:

$$\phi\left(u_k, v_l\right) = \frac{\sum_{e=0}^{p} \sum_{f=0}^{q} \varphi_{i,j}^{u,v} \; N_\alpha\left(u\right) M_\beta(v) w_{\alpha,\beta}}{\sum_{e=0}^{p} \sum_{f=0}^{q} N_\alpha\left(u\right) M_\beta(v) w_{\alpha,\beta}}, \tag{26}$$

where $\alpha = s + e - p$ and $\beta = t + f - q$. Here the parameters (s, t) are the span indices satisfying the relation:

$$\left(u, v\right) \in \left(\left[u_s, u_{s+1}\right) \times \left[v_t, v_{t+1}\right)\right). \tag{27}$$

Now substituting Equation (26) into Equation (25), leads to the computation of the control point on the $(i, j)^{th}$, mesh and the discretized form of the integral Equation for the lifting bodies is:

$$\frac{1}{2} \left\{ \frac{\sum_{e=0}^{p} \sum_{f=0}^{q} N_{\alpha_i}\left(u_i\right) N_{\beta_j}\left(v_j\right) w_{\alpha_i,\beta_j} \varphi_{\alpha_i,\beta_j}^{u,v}}{\sum_{e=0}^{p} \sum_{f=0}^{q} N_{\alpha_i}\left(u_i\right) N_{\beta_j}\left(v_j\right) w_{\alpha_i,\beta_j}} \right\} \\ + \sum_{c,d} \left\{ \iint_{S_{c,d}} \frac{\sum_{e=0}^{p} \sum_{f=0}^{q} N_\alpha\left(u_i\right) N_\beta\left(v_j\right) w_{\alpha,\beta} \varphi_{\alpha,\beta}^{u,v}}{\sum_{e=0}^{p} \sum_{f=0}^{q} N_\alpha\left(u_i\right) N_\beta\left(v_j\right) w_{\alpha,\beta}} \right\} \frac{\partial G}{\partial n} dS \\ + \sum_{d} \left\{ \iint_{S_d^w} \left(\Delta\phi\right)_\mu \frac{\partial G}{\partial n} \right\} dS = \sum_{c,d} \left\{ \iint_{S_{c,d}} G \frac{\partial \phi}{\partial n} \right\} dS, \tag{28}$$

where $\alpha_i = s_i + e - p$, $\beta_j = t_j + f - q$, $\alpha = s_v + e - p$, and $\beta = t_\mu + f - q$. It can be noticed that the (c, d) summation for the dipole over the meshes on the blade or the body surface in Equation (28) includes the case of $i = c$ and $j = d$. In the constant strength doublet mesh method this term does not come into consideration as its effect is already been taken into account by the subtended angle of the hemi-sphere surrounding the point where the potential is evaluated. However, in the higher order mesh method, there are additional effects from the curvature of the geometry and the higher order variation of the potential in addition to the subtended angle effect.

5.1 (d) Important IGA characteristics

In the NURBS based IGA, there are two meshes: the control mesh and the physical mesh. Control mesh interpolates the control points and it consists of multi-

linear elements (in 2D they are bilinear quadrilateral elements). Control mesh does not conform to the actual geometry but controls it like a scaffold. Control variables are: Degrees of freedom and they are located at the control points. These are the generalized coordinates. Control elements can be degenerated to more primitive shapes (i.e. triangle and tetrahedral, etc.). Also, control mesh can be severely distorted and even inverted to an extent, while at the same time, for sufficiently smooth NURBS, the physical geometry can be valid, which is not the case with finite elements. Important properties of the NURBS for IGA are the following:

- Mesh of a NURBS patch is defined as the tensor product of knot vectors.
- Knot intervals span the domain of the iso-geometric elements and the support for each basis function consists of a small number of elements.
- Control points associated with the basis functions define the geometry and the iso-parametric concept is invoked. Associated coefficients with the basis functions are the degrees of freedom or control variables.
- Three refinement strategies are available and the matrices and vectors associated with the elements built from iso-parametric NURBS are assembled in matrices and global vectors as in Hughes (2012).
- Specific boundary conditions are applied only to the control points and the homogeneous conditions are satisfied point-wise. In the case of inhomogeneous conditions, the boundary conditions are approximated by functions included in the NURBS function space. The condition is then satisfied in a strong but approximate way.

5.2 DE-SINGULARIZATION OF THE INDUCTION INTEGRALS

To address the singularity of induction integrals, originally an idea was proposed in Cao et al. (1991) and later it was extended by Maniar (1995). A review can be found in Cao and Beck (2015). Herein, we follow the original ideas of Cao et al. (1991), Maniar (1995) and Cao and Beck (2015) and extend their work to include the de-singularization of the induction integrals to cover all the hydrodynamic problems of interest in the present paper. And, for the sake of completeness we present these in-details.

We consider the induction integrals due to unit strength source and the doublet singularity and they are:

$$I^s = \frac{-1}{4\pi}\iint \frac{1}{r} dS \text{ , and } I^d = \frac{-1}{4\pi}\iint \frac{\vec{n}.\vec{r}}{r^3} dS. \qquad (29)$$

where dS and $\vec{n}$ are the differential element and unit normal on the surface of the integration and r is the distance between the collocation point and some field point on the surface of the body. When the collocation point falls within the mesh boundary, distance r becomes zero at some point on the mesh and hence the integral become singular, however, it is integrable.

To remove this singularity, we implement the following idea:

- The rectangular parametric space is partitioned in to four triangles as shown in Figure 6. The apex of each of the triangles is located at the collocation point and their base at the side of the edge of patch.

Then, the quadratic transformation is applied to transfer these triangles into rectangles where the apex represents the whole edge connecting ((-1, 1) and (-1, -1)). This is shown in Figure 6.

With respect to Figure 6, for the partitioned triangles $\left(\Delta^1, \Delta^2, \Delta^3 \text{ and } \Delta^4\right)$, the quadratic transformation equations are written:

(a) for the Δ^1 these are:

$$U = \frac{u_i(1+\xi)(1-\eta)}{4} + \frac{u_{i+1}(1+\xi)(1+\eta)}{4} + \frac{u(1-\xi)}{2}, \text{and}$$
$$V = \frac{v_i(1+\xi)}{2} + \frac{v(1-\xi)}{2};$$

(b) for the Δ^2 these are:

$$U = \frac{u_{i+1}(1+\xi)}{2} + \frac{u(1-\xi)}{2}, \text{ and}$$
$$V = \frac{v_i(1+\xi)(1-\eta)}{4} + \frac{v_{i+1}(1+\xi)(1+\eta)}{4} + \frac{v(1-\xi)}{2};$$

(c) for the Δ^3 these are:

$$U = \frac{u_{i+1}(1+\xi)(1-\eta)}{4} + \frac{u_i(1+\xi)(1+\eta)}{4} + \frac{u(1-\xi)}{2}, \text{ and}$$
$$V = \frac{v_{i+1}(1+\xi)}{2} + \frac{v(1-\xi)}{2};$$

(c) for the Δ^4 these are:

$$U = \frac{u_i(1+\xi)}{2} + \frac{u(1-\xi)}{2}, \text{ and}$$
$$V = \frac{v_{i+1}(1+\xi)(1-\eta)}{4} + \frac{v_i(1+\xi)(1+\eta)}{4} + \frac{v(1-\xi)}{2}. \qquad (30)$$

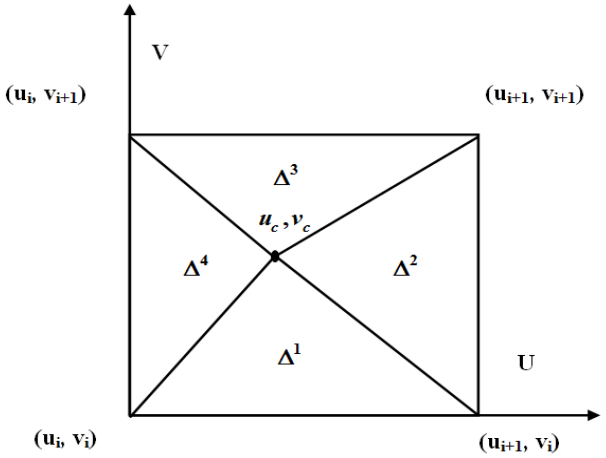

(a) Triangulation of the parametric space for de-singularization.

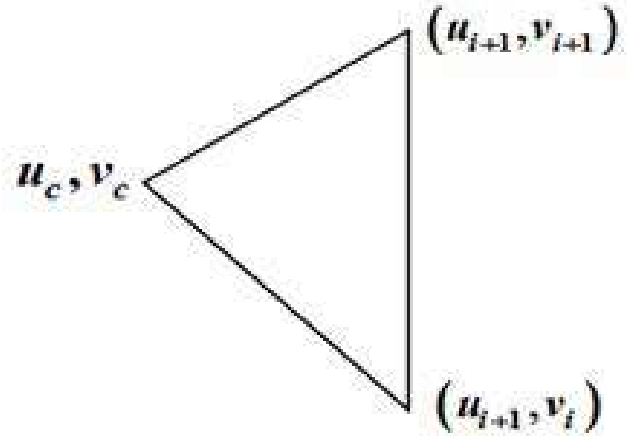

(b) De-singularized triangle.

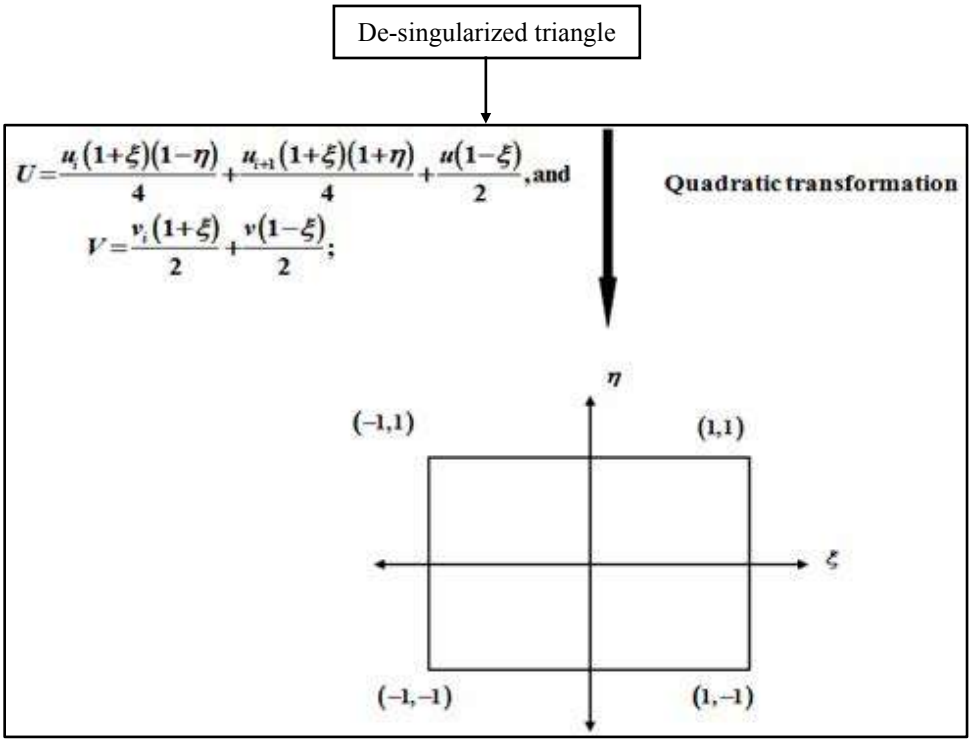

(c) Quadratic transformation of the parametric space for de-singularization.

Figure 6: Triangulation and quadratic transformation of the parametric space for de-singularization.

Now, with partitioning the integrals (Equation 29), and with the procedure mentioned above, the Equation (29) is re-written:

$$I^s = \sum_{k=1}^{4} \frac{-1}{4\pi} \iint_{\Delta^k} \frac{1}{r} J_c \; d\xi \; d\eta \; ,$$
$$I^d = \sum_{k=1}^{4} \frac{-1}{4\pi} \iint_{\Delta^k} \frac{\vec{n}.\vec{r}}{r^3} J_c \; d\xi \; d\eta \; , \tag{31}$$

where J_c is the Jacobian of the surface element ds and it is evaluated:

$$J_c = \left| \frac{\partial \vec{r}}{\partial \xi} \times \frac{\partial \vec{r}}{\partial \eta} \right|, \tag{32}$$

and the unit normal vector to surface of the element is:

$$\vec{n} = \frac{\frac{\partial \vec{r}}{\partial \xi} \times \frac{\partial \vec{r}}{\partial \eta}}{J_c}. \tag{33}$$

The more computational details about de-singularization can be found in Goel (2016).

5.3 SELF-INDUCED POTENTIAL FUNCTION OF THE DIPOLES AND THE SOURCE OF HIGHER ORDER

When the collocation point falls on mesh surface, the induction integral due to the normal dipole of the higher order requires a special treatment as described in Section 5.2. The contribution of higher order is, however, less singular than that due to the constant term in the dipole strength. Hence, the dipole induced potential of higher order is computed:

$$I^s = \sum_{k=1}^{4} \frac{-1}{4\pi} \iint_{\Delta^k} \frac{1}{r} J_c \; d\xi \; d\eta \text{ , and}$$
$$I^d = \sum_{k=1}^{4} \frac{-1}{4\pi} \iint_{\Delta^k} \frac{\vec{n}.\vec{r}}{r^3} J_c \; d\xi \; d\eta \; . \tag{34}$$

Now, substituting the NURBS representation for potential function from Equation (26) in Equation (34), we obtain:

$$I^d = \sum_{k=1}^{4} \frac{-1}{4\pi} \iint_{\Delta^k} \left[\frac{\sum_{e=0}^{p} \sum_{f=0}^{q} \varphi_{\alpha,\beta}^{u,v} N_\alpha(u) M_\beta(v) w_{\alpha,\beta}}{\sum_{e=0}^{p} \sum_{f=0}^{q} N_\alpha(u) M_\beta(v) w_{\alpha,\beta}} \right] \left(\frac{-\vec{n}.\vec{r}}{r^3} \right) J_c \; d\xi \; d\eta. \tag{35}$$

For Equation (35), the Gauss quadrature is used for the numerically integration as the singularity has been eliminated using the transformation discussed in Section 5.2. Now, the self-induced potential of higher order source is numerically computed:

$$I^s = \sum_{k=1}^{4} \frac{-1}{4\pi} \iint_{\Delta^k} \left(-\frac{\partial \phi}{\partial n} \right) \frac{1}{r} J_c \; d\xi \; d\eta \; . \tag{36}$$

In both the integrations, the Jacobian and normal vectors are computed using the transform Equations (32) and (33) respectively.

5.4 NEAR FIELD INFLUENCE COEFFICIENT COMPUTATIONS VIA THE ADAPTIVE SUB-DIVISION TECHNIQUE FOR NURBS

Following Maniar (1995), we consider the problem of evaluating source and dipole integrals and their moments:

$$\iint f(u,v) \; J_c \; du \; dv \; , \tag{37}$$

when the field point lies in near field range of a curved surface. In Equation (37), the $f(u,v) = u^m v^n / R$ is for the source integrals, the $f(u,v) = u^m v^n \vec{n}.(1/R)$ is for dipole integrals and the J_c is Jacobian of the transformation. If, the $d / L \geq 1$, then the field point is in the near field range of the surface, where d is some representative length scale of the surface and L is the distance of the centroid of surface from the field point, Figure 7a. When the $d/L << 1$, than the numerical experimentation indicates that a $(N_g \times N_g)$ Gauss-Legendre product rule, where $3 \leq N_g \leq 5$, performs well with an absolute error $\leq 1 \times 10^{-5}$, i.e.

$$\iint f(u,v) J \; du \; dv \cong \sum_{k=1}^{N_g} \sum_{k=1}^{N_g} w_i w_j \; f(u_i, v_j) \; J_c(u_i, v_j). \tag{38}$$

Primarily, the choice of order N_g is dependent on the ratio of d/L and the largest degree of the influence coefficients required. For the low curvature surfaces, the choice of the order is only weakly dependent on the geometry of the surface. Implicit in the requirement, $d/L << 1$ is the fact that the smaller it is, the smoother the functional variation of the Rankine singularity $1/R$, over the surface of integration will be. The above observation suggests that, when the field point is in the near field (i.e. $d/L \geq 1$) domain, we can subdivide the surface sufficiently such that for each of the sub-divided surfaces $d/L << 1$ (Figures 6 and 7a), and a $(N_g \times N_g)$ Gauss-Legendre product rule can be applied to each of the subdivided surfaces for the numerical integration. For computational efficiency, the reduction in the ratio d/L is important and it has been done effectively and selectively in the sub-division used in this paper, i.e. the scheme is adaptive.

The procedure is outlined with reference to Figure 7a and it is:

- Choose a constant where $0 < \chi < 1$, and given a field point and a surface, evaluate (d/L) and if:
- $(d/L) > \chi$ then subdivide the surface, and
- $(d/L) \leq \chi$ then no subdivision is required.

If no subdivision is required, the integral is integrated using a $(N_g \times N_g)$ Gauss-Legendre product rule. For each of the subdivided surface the ratio (d/L) is evaluated and the above criteria is checked. If the criteria are not satisfied, the surface is further sub-divided. It is obvious that the procedure is inherently recursive and will continue until no further subdivision is required. In computational practice, L is evaluated as shown in Figure 7a. Here, the several combinations of N_g and (d/L) are numerically experimented. And, based upon the experimentation the $N_g = 4$ and $(d/L) \leq 0.4$, is found to be an optimal choice ensuring an absolute error close to 1×10^{-6}. Table 2 shows the relative error in computation with varying values of α. It can be noted from Table 2 that when $\chi \leq 0.4$ the absolute error is approximately close to 1×10^{-6}.

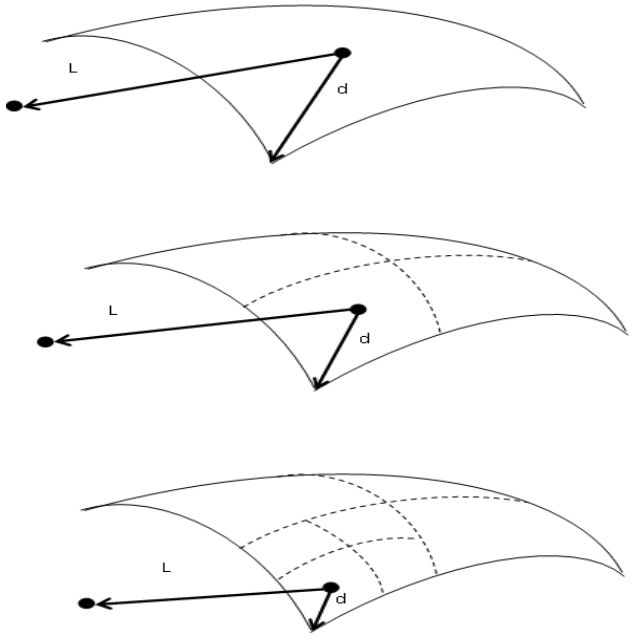

(a) Definition of the length-wise scale and sub-division of the surface patch.

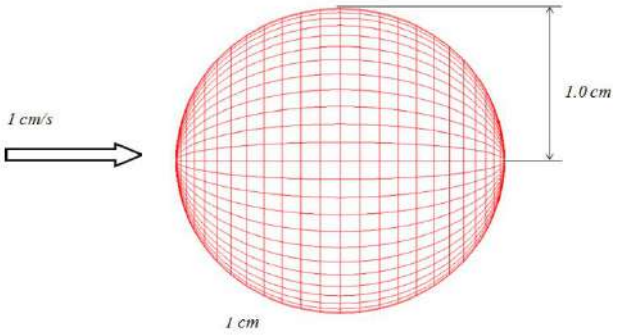

(b) Definition of the geometry and the panel distribution for surface of the sphere.

Figure 7: Definition of the length-wise scale and sub-division of the surface patch and definition of the geometry and the mesh distribution for surface of the sphere.

5.5 IMPOSITION OF KUTTA CONDITION

For any lifting flow problem, the Kutta condition needs to be satisfied at the trailing edge of lifting surface. The Kutta condition can be satisfied either by linear method as suggested by Morino & Kuo (1974) or by satisfying the non-linear zero pressure jump condition. According to Morino & Kuo (1974), the strength of wake sheet dipole at any potential control vortex is equivalent to potential jump at the trailing edge on the same radial control vortex, i.e.

$$\Delta\phi_j^v = \Delta\phi_j^{+v} - \Delta\phi_j^{-v} = \Delta\phi_{N^v-1,j}^v - \Delta\phi_{0,j}^v \tag{39}$$

where the superscripts + and – denote the suction and pressure sides of the trailing edge. Another form of the Kutta condition is satisfied by equating the magnitude of velocities of the flow at trailing edge of the surface, i.e.

$$\left(\overrightarrow{U_r} + \nabla\phi^+\right)^2 = \left(\overrightarrow{U_r} + \nabla\phi^-\right)^2 \tag{40}$$

where $\overrightarrow{U_r} = (U,V,W)$ and $\nabla\phi = (\partial\phi/\partial x, \partial\phi/\partial y, \partial\phi/\partial z)$. Expanding the above equation and re-arranging we get:

$$\left\{\begin{array}{l}\dfrac{\partial\phi}{\partial x}\left(2U+\dfrac{\partial\phi}{\partial x}\right)+\dfrac{\partial\phi}{\partial y}\left(2V+\dfrac{\partial\phi}{\partial y}\right)\\ +\dfrac{\partial\phi}{\partial z}\left(2W+\dfrac{\partial\phi}{\partial z}\right)\end{array}\right\}^+ - \left\{\begin{array}{l}\dfrac{\partial\phi}{\partial x}\left(2U+\dfrac{\partial\phi}{\partial x}\right)+\dfrac{\partial\phi}{\partial y}\left(2V+\dfrac{\partial\phi}{\partial y}\right)\\ +\dfrac{\partial\phi}{\partial z}\left(2W+\dfrac{\partial\phi}{\partial z}\right)\end{array}\right\}^- = 0 \tag{41}$$

Equation (41) is a non-linear equation in perturbation velocity and therefore iterative procedure is required to solve the equation. At any step, we can write term of Equation (41):

$$A = \left(2U+\frac{\partial\phi}{\partial x}\right)^{t-1}, B = \left(2V+\frac{\partial\phi}{\partial y}\right)^{t-1}, \quad C = \left(2W+\frac{\partial\phi}{\partial z}\right)^{t-1} \tag{42}$$

After re-arranging, we can write Equation (41):

$$\left\{\begin{array}{l}\dfrac{1}{D}\begin{vmatrix} A & B & C \\ \dfrac{\partial\phi}{\partial v} & \dfrac{\partial y}{\partial v} & \dfrac{\partial z}{\partial v} \\ n_0 & n_1 & n_2 \end{vmatrix}\dfrac{\partial\phi}{\partial u} + \dfrac{1}{D}\begin{vmatrix} \dfrac{\partial\phi}{\partial u} & \dfrac{\partial y}{\partial u} & \dfrac{\partial z}{\partial u} \\ A & B & C \\ n_0 & n_1 & n_2 \end{vmatrix}\dfrac{\partial\phi}{\partial v}\\ +\dfrac{1}{D}\begin{vmatrix} \dfrac{\partial\phi}{\partial u} & \dfrac{\partial y}{\partial u} & \dfrac{\partial z}{\partial u} \\ \dfrac{\partial\phi}{\partial v} & \dfrac{\partial y}{\partial v} & \dfrac{\partial z}{\partial v} \\ A & B & C \end{vmatrix}\dfrac{\partial\phi}{\partial n}\end{array}\right\}^+ - \left\{\begin{array}{l}\dfrac{1}{D}\begin{vmatrix} A & B & C \\ \dfrac{\partial\phi}{\partial v} & \dfrac{\partial y}{\partial v} & \dfrac{\partial z}{\partial v} \\ n_0 & n_1 & n_2 \end{vmatrix}\dfrac{\partial\phi}{\partial u} + \dfrac{1}{D}\begin{vmatrix} \dfrac{\partial\phi}{\partial u} & \dfrac{\partial y}{\partial u} & \dfrac{\partial z}{\partial u} \\ A & B & C \\ n_0 & n_1 & n_2 \end{vmatrix}\dfrac{\partial\phi}{\partial v}\\ +\dfrac{1}{D}\begin{vmatrix} \dfrac{\partial\phi}{\partial u} & \dfrac{\partial y}{\partial u} & \dfrac{\partial z}{\partial u} \\ \dfrac{\partial\phi}{\partial v} & \dfrac{\partial y}{\partial v} & \dfrac{\partial z}{\partial v} \\ A & B & C \end{vmatrix}\dfrac{\partial\phi}{\partial n}\end{array}\right\}^- = 0 \tag{43}$$

From Equation (43), we note that the non-linear Kutta condition is expressed by linear combinations of the potential vertices.

5.6 SOLUTION OF THE LINEAR SYSTEM OF EQUATIONS

Herein, we use the collocation method to construct linear system of equations. In case of the 'Constant Strength Mesh Method (CSPM)', only a single collocation point is selected at the centroid of each of the meshes. Therefore the numbers of unknown are $(N-p)\times(M-q)$, where N and M are the number of data points in the u and v parametric directions respectively, and p and q are the degree of the surface in u and v parametric directions respectively. The simple Gauss elimination method is used to solve this linear system of algebraic equations. However, in case of the 'Higher Order Mesh Method (HOPM)', the number of unknowns $N\times M$ are greater than the number of meshes $\left(N^\phi - p\right)\times\left(M^\phi - q\right)$. Thus, to produce the enough number of equations, more number of collocation points is placed at each of the meshes, and where the no penetration kinematic boundary condition on the body surface is satisfied.

In the present paper, four collocation points are selected per mesh at the intersections of $\xi = 0.5$ and -0.5 and $\eta = 0.5$ and -0.5, when the mesh boundaries are limited

by the normalized local parameters $(\xi = 1 \text{ and } -1)$ and $(\eta = 1 \text{ and } -1)$. Thus, the total number of equations is $4\times\left(N^{\phi} - p\right)\times\left(M^{\phi} - q\right)$. Equation (28) is solved for the unknown velocity potentials by Lagrange multipliers using Equation (43) as constraint, for more details see Goel (2016) and Lee & Kerwin (2003).

5.7 COMPUTATION OF VELOCITIES, PRESSURE, FORCES AND MOMENTS

Once the potential function values are determined by solving the linear system of equations, the surface velocities can be computed by the numerical differentiation of potential function or by direct computation of the source and the doublet mesh influence functions. The method of computing the velocities by direct computation of the source and the doublet mesh influence functions is generally not adopted, as the influence functions for the velocities computations are more singular and therefore more sensitive to the position of the field point within each mesh. In the case of CSPM, any numerical differentiation technique can be used to compute the velocities. In the present paper, for the CSPM, second order differential method is used to compute the tangent perturbation velocity in the orthogonal directions. In addition, the total tangential velocity is obtained by a vector sum of the perturbation velocity and the undisturbed inflow velocity. In the case of HOPM to obtain the perturbation velocity, the derivative of the perturbation potential function is taken with respect to the physical coordinates. As in the present formulation physical coordinates $\bar{x}$ and the perturbation potential function ϕ both are functions of parametric directions (u,v), the chain rule is used to get:

$$\begin{aligned}
\frac{\partial\phi}{\partial u} &= \frac{\partial\phi}{\partial x}\frac{\partial x}{\partial u} + \frac{\partial\phi}{\partial y}\frac{\partial y}{\partial u} + \frac{\partial\phi}{\partial z}\frac{\partial z}{\partial u},\\
\frac{\partial\phi}{\partial v} &= \frac{\partial\phi}{\partial x}\frac{\partial x}{\partial v} + \frac{\partial\phi}{\partial y}\frac{\partial y}{\partial v} + \frac{\partial\phi}{\partial z}\frac{\partial z}{\partial v},\\
\frac{\partial\phi}{\partial n} &= \frac{\partial\phi}{\partial x}\frac{\partial x}{\partial n} + \frac{\partial\phi}{\partial y}\frac{\partial y}{\partial n} + \frac{\partial\phi}{\partial z}\frac{\partial z}{\partial n},\\
\text{or } \frac{\partial\phi}{\partial n} &= \frac{\partial\phi}{\partial x}n_0 + \frac{\partial\phi}{\partial y}n_1 + \frac{\partial\phi}{\partial z}n_2,
\end{aligned} \tag{44}$$

where $\bar{x} = (x, y, z)$ and $\vec{n} = (n_0, n_1, n_2)$. The derivatives of $\bar{x}$ with respect to the parameters (u,v) can be computed easily. The derivatives of ϕ with respect to the parameters (u,v) can be computed similarly as the derivatives of the physical coordinates are computed. The normal component of the perturbation $(\partial\phi/\partial n)$ is known from the kinematic condition. Now, using the Kramer's rule, Equation (44) is solved for the perturbation velocity components:

$$\frac{\partial\phi}{\partial x} = \frac{1}{D}\begin{vmatrix} \frac{\partial\phi}{\partial u} & \frac{\partial y}{\partial u} & \frac{\partial z}{\partial u} \\ \frac{\partial\phi}{\partial v} & \frac{\partial y}{\partial v} & \frac{\partial z}{\partial v} \\ \frac{\partial\phi}{\partial n} & n_1 & n_2 \end{vmatrix}, \frac{\partial\phi}{\partial y} = \frac{1}{D}\begin{vmatrix} \frac{\partial x}{\partial u} & \frac{\partial\phi}{\partial u} & \frac{\partial z}{\partial u} \\ \frac{\partial x}{\partial v} & \frac{\partial\phi}{\partial v} & \frac{\partial z}{\partial v} \\ n_0 & \frac{\partial\phi}{\partial n} & n_2 \end{vmatrix}, \tag{45}$$

$$\frac{\partial\phi}{\partial y} = \frac{1}{D}\begin{vmatrix} \frac{\partial x}{\partial u} & \frac{\partial y}{\partial u} & \frac{\partial\phi}{\partial u} \\ \frac{\partial x}{\partial v} & \frac{\partial y}{\partial v} & \frac{\partial\phi}{\partial v} \\ n_0 & n_1 & \frac{\partial\phi}{\partial n} \end{vmatrix},$$

where the determinant D is defined:

$$D = \begin{vmatrix} \frac{\partial x}{\partial u} & \frac{\partial y}{\partial u} & \frac{\partial z}{\partial u} \\ \frac{\partial x}{\partial v} & \frac{\partial y}{\partial v} & \frac{\partial z}{\partial v} \\ n_0 & n_1 & n_2 \end{vmatrix}. \tag{46}$$

As the flow is assumed to be the potential flow, the Bernoulli's equation is used to compute the non-dimensional pressure coefficient:

$$C_p = \frac{P - P_\infty}{0.5\times\rho\times {U_\infty}^2}, \tag{47}$$

where $P - P_\infty$ is replaced with $P - P_\infty = \frac{1}{2}(U^2 - {U_\infty}^2)$. Therefore, Equation (47) is reduced to:

$$C_p = 1 - \left(\frac{U^2}{{U_\infty}^2}\right). \tag{48}$$

Total forces and moments are obtained by the summation of individual mesh force vectors. At last, the integrated thrust and the torque coefficients are computed:

$$K_T = \frac{T}{\rho n^2 D^4} = \frac{J^2}{8} K \sum_i \frac{A_i}{R^2}\left(C_p\right)_i \left(n_x\right)_i, \tag{49}$$

$$K_Q = \frac{Q}{\rho n^2 D^5} = \frac{J^2}{16} K \sum_i \frac{A_i}{R^2}\left(C_p\right)_i \left[\left(n_y\right)_i \frac{z_i}{R} - \left(n_x\right)_i \frac{y_i}{R}\right], \tag{50}$$

where x_i, y_i, z_i are the physical coordinates; $\left(n_x\right)_i, \left(n_y\right)_i, \left(n_z\right)_i$ are the components of unit normal vector to surface of the body or the mesh under

consideration; A_i is the area of the i^{th} mesh; and K is the number of symmetries. For the efficient computation, these summations are performed individually over the blade and hub surfaces.

6. RESULTS AND DISCUSSIONS

We develop two separate software programs for the following problems:

- Wing section of a NACA 0012 aerofoil and the non-lifting problems, and
- Un-skewed propeller (DTMB 4119) and skewed propeller (DTNSRDC 4382).

All the formulations are based upon iso-geometric analysis as in it an integration of the hydrodynamic analysis model is achieved with the conventional NURBS-based computer aided geometric design model of propeller. Herein, in all the examples we either use quadratic or cubic degrees and multiple patches. Patches are joined with C^1 (derivational tangent plane continuity) using standard techniques as defined in Farin (1999), Piegl and Tiller (1996), and Roger and Adams (2017). We use the centripetal parametrization from Lee (1989) and knot vectors are generated through the laws of average (de Boor 2001) with clamped and/or closed end conditions.

6.1 PROBLEM 1: FLUID FLOW OVER A SPHERE

Potential fluid flow past over a sphere is chosen as the first example because the analytical results for this simple flow problem are available from the literature, for details see Anderson (2007). The coordinate system and the mesh arrangement for the sphere geometry are shown in Figure 7b. In the mesh geometry, the cosine spacing is chosen in both the directions to account for the rapid changes in the geometry and the singularity near the edges of the geometry. The analytical expressions for the perturbation potential function and the total surface velocity at the center plane of sphere are:

$$\phi = 0.5 \times r \times \cos(\theta), U = U_\infty \times 1.5 \times \sin(\theta), \qquad (51)$$

where θ is the azimuth angle and U_∞ is the undisturbed free stream velocity. Figures 8a, 8b, 9a, and 9b show the comparison of chord-wise potential function, velocity distribution and pressure coefficient distribution respectively between the analytical solution, CSPM and QHOPM. From the presented results, we observe that the computed potential function and surface velocities are in good agreement with the analytical results, with the maximum error being close to 1×10^{-3} only. As the maximum error is extremely low, the curves are merging in Figures 8a, 8b, 9a, and 9b, e.g. they are over lapping for the analytical, CSPM and QHOPM.

Since the velocity in CSPM is computed by a difference formula from the potential function, a small error in the potential function distribution can be magnified in the velocity function distribution, but the effect of these errors is localized. In the case of HOPM, the surface velocities are computed using chain rule and hence they are more accurate and easy to compute as compared to the CSPM. In Figures 9b and 10a, the comparison has been made between CSPM and QHOPM for the maximum error in perturbation potential function and surface velocity computations. And, we see that the QHOPM converges faster as compared to the CSPM.

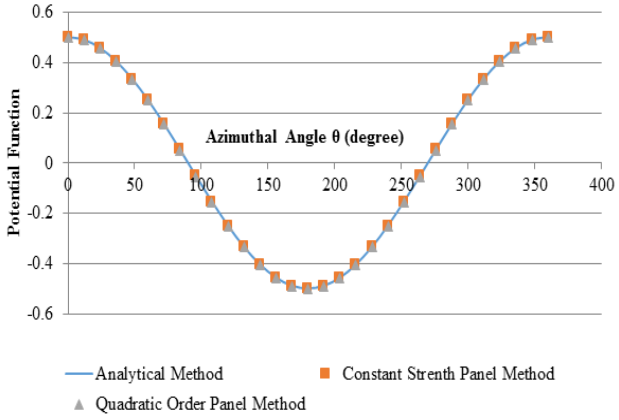

(a) Computed perturbation potential function at the center plane of sphere using the CSPM and QHOPM.

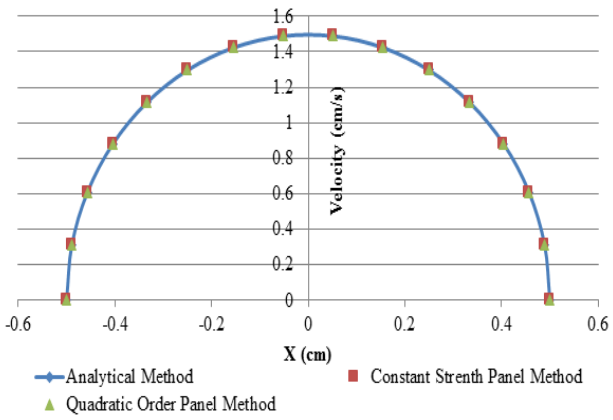

(b) Computed surface velocity at the center plane of sphere using the CSPM and QHOPM.

Figure 8: Computed perturbation potential function and surface velocity at the center plane of sphere using the CSPM and QHOPM.

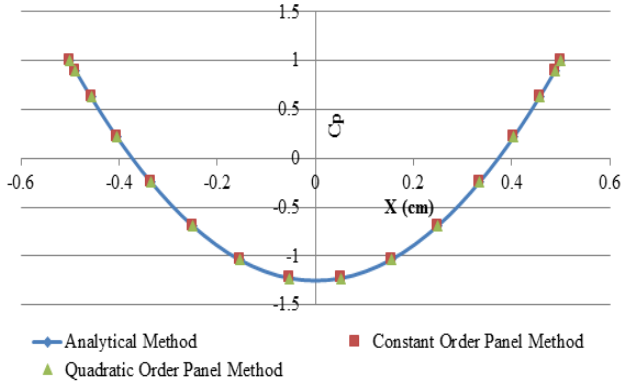

(a) Computed pressure coefficient distribution at the center plane of sphere using CSPM and QHOPM.

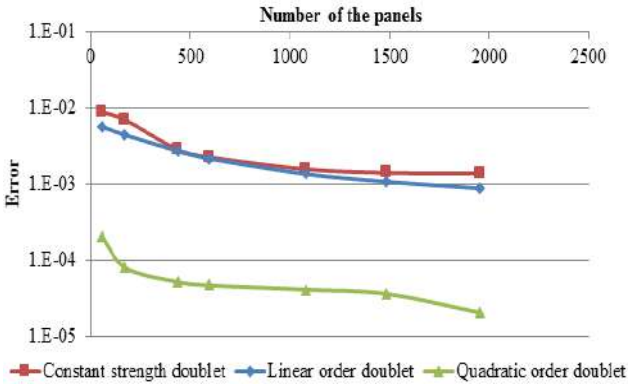

(b) Comparative study of the CSPM and QHOPM with respect to the maximum error in estimation of the potential function.

Figure 9: Computed pressure coefficient distribution at the center plane of sphere using CSPM and QHOPM and comparative study of the CSPM and QHOPM with respect to the maximum error in estimation of the potential function.

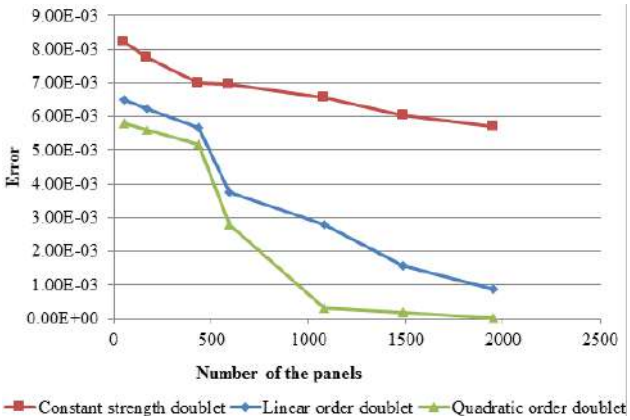

(a) Comparative study between the CSPM and QHOPM with respect to the maximum error in estimation of the velocity.

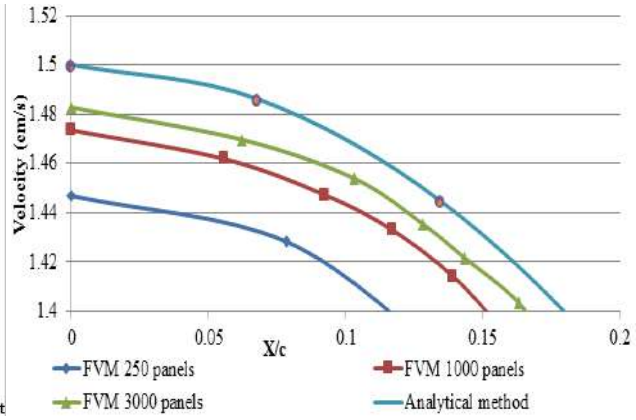

(b) Computational comparison between the BEM of present paper and the FVM (Ansys-Fluent^{**TM}).

Figure 10: Comparative study between the CSPM and HOPM with respect to the maximum error in estimation of the velocity and computational comparison between the BEM of present paper and the FVM (Ansys-Fluent^{**TM}).

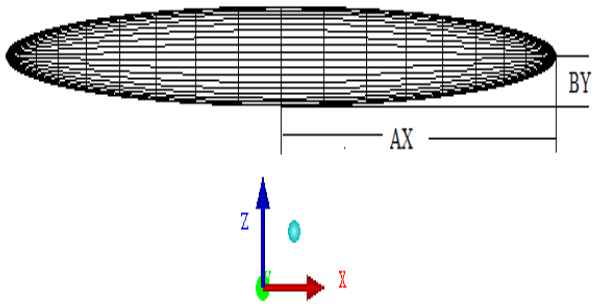

(a) Definition of the geometry and panel distribution for ellipsoid.

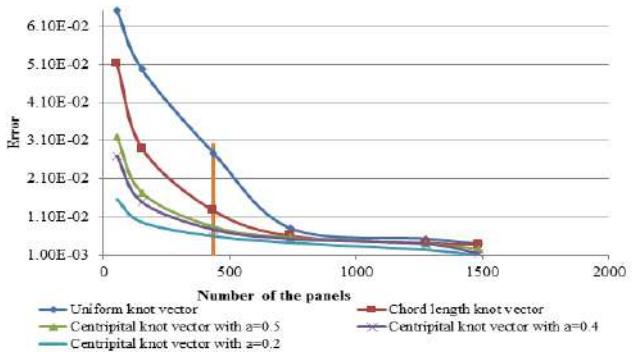

(b) Comparative study on the effect of selection of knot vector on computational analysis.

Figure 11: Definition of the geometry and mesh distribution for ellipsoid and comparative study on the effect of selection of knot vector on computational analysis.

Furthermore, Table 3 and Figure 10b show the comparison of mesh methods with 'Finite Volume Method (FVM) – in Fluent**TM). From the results we notice that for the potential flow problems, the 'Boundary Element Method (BEM)' converges faster as compared to the FVM and the computational costs involved in the BEM is very less as compared to the FVM for the same level of desired accuracy.

6.2 PROBLEM 2: EFFECT OF THE KNOT VECTOR SELECTION ON ANALYSIS

We consider the QHOPM and potential fluid flow past an ellipsoid with semi-lengths of its axes are given as AX=1.0, BY=0.2, and CZ=0.2. Figure 11a shows the mesh arrangement and geometry of ellipsoid. The maximum error in the surface velocity distribution over the center plane of ellipsoid for the different knot vectors is plotted in Figure 11b. Following Schlichting (1955), the analytical expression for velocity at the centre plane of ellipsoid is:

$$\frac{U_{surf}}{U_{\max}} = \sqrt{\frac{1-x^2}{1-x^2y^2}}, \tag{52}$$

with $y = \sqrt{1-r^2}$ and x is the distance from the midpoint in units so that the length is 2, and r is the radius and the maximum surface velocity is:

$$\frac{U_{\max}}{U_{\infty}} = \frac{2}{2-B}, \tag{53}$$

where $B = \frac{2(1-y^2)}{y^3}(\tanh^{-1} y - y)$. From results of Figure 11b, we conclude that the centripetal method with a small value of centripetal parameter coefficient 'a' provides a tighter and efficient representation of the surface and results into higher accuracy in the potential function computations.

6.3 PROBLEM 3: FLUID FLOW OVER A RECTANGULAR WING SECTION OF A NACA 0012 AEROFOIL

We consider fluid flow over a rectangular wing (i.e. of NACA 0012 section). The numerical simulation is performed for the 5 degrees angle of attack with an aspect ratio of 5. The results are compared with results obtained from the FVM (Fluent**TM). The coordinate system and mesh arrangement for the problem are shown in Figure 12. Here, the QHOPM code is used and the analysis is performed for the same problem with different number of meshes both in the chord-wise and span-wise directions. Here, we find that the span-wise convergence is relatively slow compared to chord-wise convergence because of the low aspect ratio of wing section. The results show that our QHOPM - BEM is converging with 20 chord-wise meshes and 25 span-wise meshes.

Because this is a lifting problem, the 'Kutta' condition is applied at the trailing edge. In case of the lifting problem there is a vortex formation at the trailing edge of the wing or any lifting surface, and that can result in the formation of strong trailing edge vortices shedding from the tip of the wing. Due to the formation of these vortices, there is a downwash component of the velocity, and that can affect the pressure distribution over the wing and hence the lift and drag forces. The shape of these vortices changes with the angle of attack, and therefore the geometry of wake is also of primary concern for the correct imposition of the Kutta condition and for accurate prediction of the propeller dynamics or the lifting flow characteristics. Herein, the wake surface is being aligned numerically by imposing a zero force condition on the wake surface. To compute the shape of the wake surface numerically, it is important, first to compute the perturbation velocity at the wake grid points and then to move the meshes of the wake sheet using the Lagrangian scheme.

Following, Morino & Kuo (1974), in order to compute the aligned wake surface, we use a relaxation algorithm. To accelerate the iteration process, an over-relaxation scheme is used for the first iteration and implemented after the first iteration is done. The algorithm consists of following steps:

- Solve the boundary value problem using an arbitrary wake shape.
- Compute the induced velocities at the collocation points of the first row and then move it to the second row using Euler scheme as keeping free stream coordinate as constant. This is written:

$$\begin{aligned} y_{m,i} &= y_{m,i-1} + \left(\nabla\phi_{m,i} + V_{\infty}\right)\times\Delta t_i, \\ z_{m,i} &= z_{m,i-1} + \left(\nabla\phi_{m,i} + V_{\infty}\right)\times\Delta t_i, \end{aligned} \tag{54}$$

  where $\Delta t_i = \left(\Delta x / |U|\right)$, and for the planner wing $\left(U = U_{\infty} + U_{induced}\right)$ and for the propeller case $\left(U_T = U_{\infty} + U_{induced} + \overline{\Omega}\times\overline{r}\right)$.

- Adjust the downstream wake shape so that it has the same shape as of the previous row, i.e. impose $y_{m,k} = y_{m,i}$ and $z_{m,k} = z_{m,i}$, where $k = i+1 \ldots N_w$.
- Repeat Steps 2 and 3 until the last row of the wake surface.
- Now for the second iteration onwards all the meshes are moved at the same time and iterations are done until the convergence is achieved.

Figures 12b, 12c, 12d, and 12e show the wake structure at the 7th, 11th, 15th and 20th iterations respectively. The computed velocity distribution over wing sectional surface of NACA 0012 aerofoil and its comparison with Fluent**TM are shown in Figure 12f.

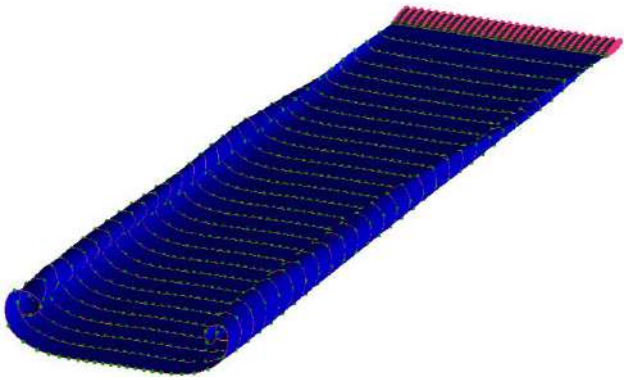

(a) Definition of the wing geometry of NACA 00215 aerofoil section with wake structure and panel distribution.

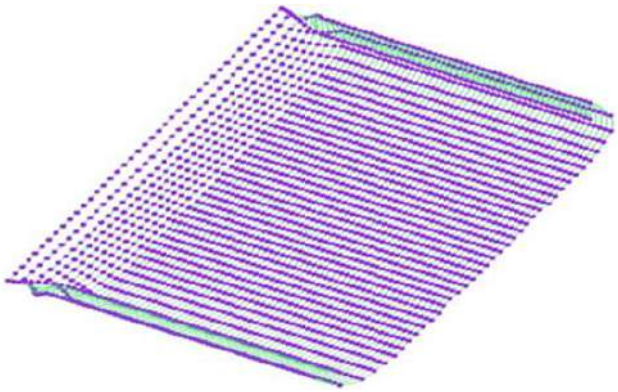

(b) Computed wake structure at the end of 7th iteration of the wing NACA 00215 aerofoil section.

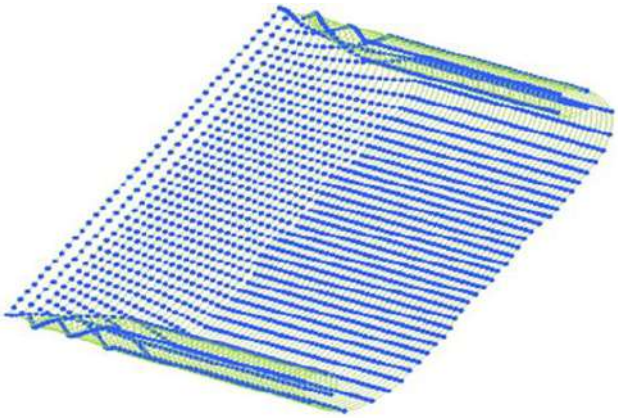

(c) Computed wake structure at the end of 11th iteration of the wing NACA 00215 aerofoil section.

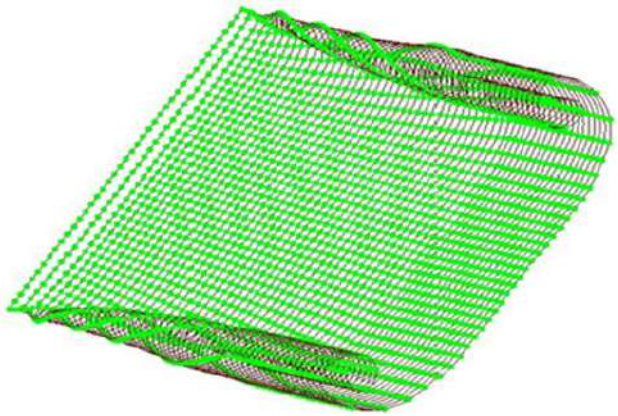

(d) Computed wake structure at the end of 15th iteration of the wing NACA 00215 aerofoil section.

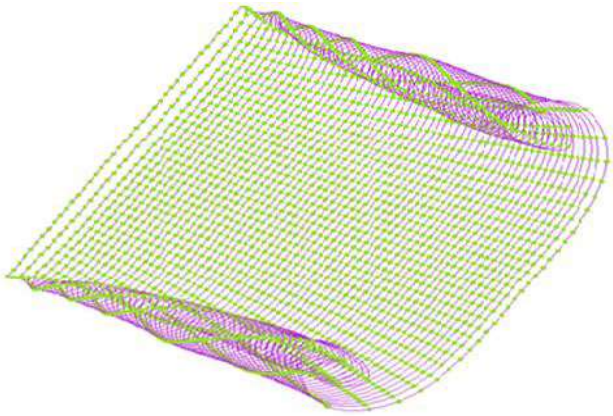

(e) Computed wake structure at the end of 20th iteration of the wing NACA 00215 aerofoil section.

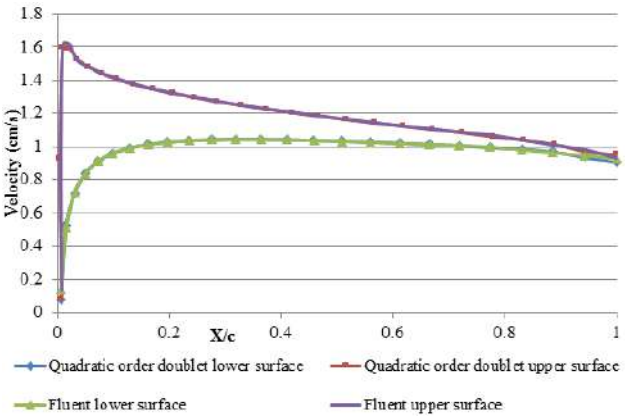

(f) Computed velocity distribution over the wing geometry of NACA 00215 aerofoil section.

Figure 12: Definition of the wing geometry of NACA 00215 aerofoil section with wake structure and mesh distribution, computed wake structure at the end of 7th, 11th, 15th and 20th iterations, and computed velocity distribution.

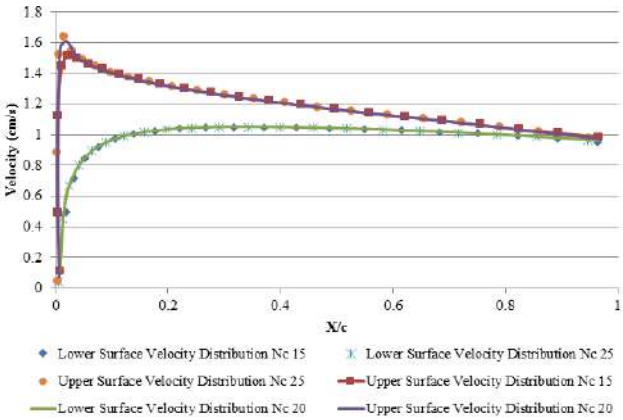

(a) Convergence of the computed velocity distribution over wing geometry of NACA 00215 aerofoil section.

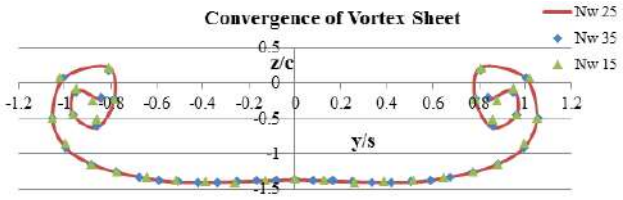

(b) Convergence of the trailing edge vortex sheet behind wing geometry of NACA 00215 aerofoil section.

Figure 13: Convergence of the computed velocity distribution over and trailing edge vortex sheet behind the wing geometry of NACA 00215 aerofoil section.

From Figure 12f, we observe that the results are in good agreement with the FVM results (Fluent**TM) with a little discrepancy near the trailing edge. This discrepancy at the trailing edge is due to the viscous effects which cannot be exactly considered by the present QHOPM-BEM as it is based on the potential flow assumptions. Figures 13a and 13b show the convergence of velocity distribution and the trailing edge vortex sheet with increasing number of meshes. The alignment algorithm shows the good convergence properties with respect to parameters governing the wake and wing discretization. From the results it can be noted that with an increase in longitudinal and transversal number of mesh, tip roll-up is better.

6.4 PROBLEM 4: STEADY STATE PERFORMANCE OF AN UN-SKEWED PROPELLER (DTMB 4119 PROPELLER)

Herein, we consider the steady state flow around an un-skewed marine propeller on axi-symmetric hub. We use the 'David Taylor Model Basin (DTMB) 4119' propeller because for this propeller the experimental results are available from Jessup (1989). The particulars of the propeller are listed in Table 1. The DTMB 4119 propeller is a three bladed propeller. The propeller blades are un-skewed with a zero degree rake angle and the section shape of the blade is a NACA 66 modified thickness form, superimposed on a mean camber line. The geometry of hub is elliptical. Since, the geometry and loading is repeated identically on each of the blades and on each of the hub segments, only one third of the geometry needs to be discretized. Only the twelve span-wise meshes are arranged to be denser towards the tip, and each strip contains 23 upper and lower surface meshes. The mesh arrangement and the body of the propeller are shown in Figure 14a.

We compute the performance of propeller for five different advance ratios and the pressure distribution over the blade surface at three different radial locations. The results are compared with the experimental results of Jessup (1989) and the measured (Jessup (1989)) and computed open water characteristics are shown in Figures 14b, 15a, 15b, 15c, 15d, 15e and 15f.

Agreement between the experimental and computational results is found to be satisfactory, except near the trailing edge. Tables 4, 5, and 6 list the computed pressure coefficient on the pressure and suction sides at different values of r / R, and compare the computed values with experimental values (Jessup (1989)) in terms of absolute error. From Figure 14b, it can be noted that there is a difference between the present BEM and experimental results and that is due to the high viscous effects around the hub of the propeller (i.e. viscous effects are strong near the hub). As the BEM is based on potential flow theory, it is difficult to compute very accurate results near the hub sections.

From Figures 15a and 15b, it can be observed that the agreement in pressure distribution is good between the experiment and present BEM. The main significant difference between the results arises near the leading edge where the pressure varies drastically from the stagnation pressure to some finite pressure. In the Figure 15b, the pressure distribution on the lower surface of the blade near the trailing edge is flat in the experiment whereas it is having convex shape in the numerical computation. This error may be due to the error in measurement or in data processing. The open water characteristics are compared, and shown in Figure 15c.

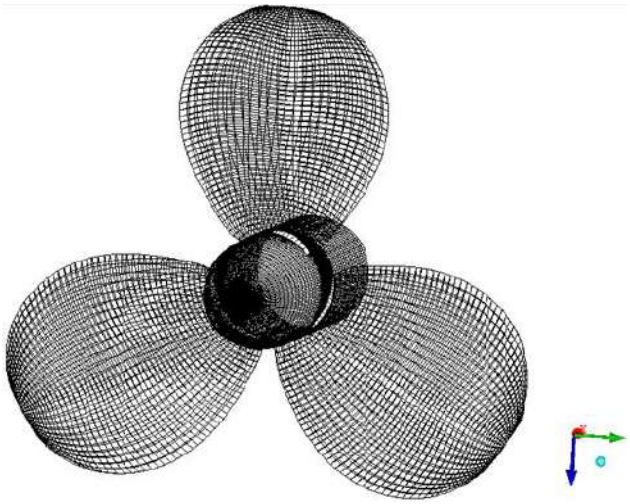

(a) Definition of the geometry and surface panel distribution for DTMB 4119 propeller.

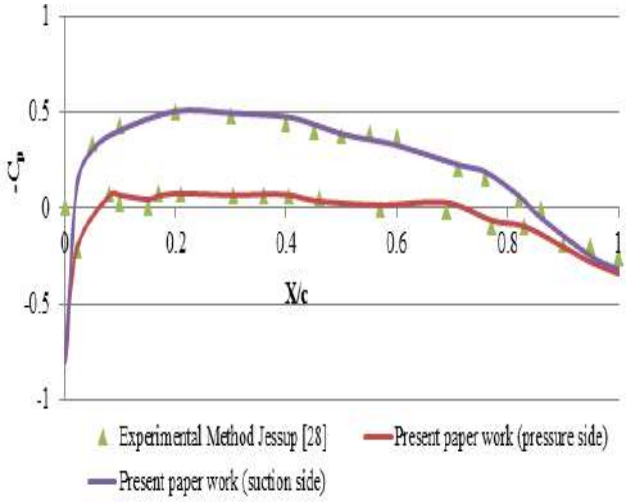

(b) Computed pressure coefficient distribution for DTMB 4119 propeller at r/R =0.3 and J=0.833 and its comparison with Jessup (1989).

Figure 14: Definition of the geometry, surface mesh distribution, computed pressure coefficient distribution for DTMB 4119 propeller at r/R =0.3 and J=0.833 and its comparison with experimental results of Jessup (1989).

Performance of the propeller is studied at different advance ratios and the absolute errors are presented in Tables 4, 5, and 6. It can be seen from Figure 15c that results are in good agreement with experimental results except at the J=0.5. At the J=0.5, this discrepancy is due to the increase in the drag due to flow separation at low advance ratio's and since primarily this is a viscous phenomenon it cannot be captured easily with the BEM.

Figures 15d, 15e, 15f and 16 show the convergence of pressure distribution on different radial locations and open water characteristics with increasing number of meshes. From the results, we note that they show good convergence with 23 chord-wise and 12 span-wise mesh distribution except at near radii (r/R=0.3).

6.5 PROBLEM 5: STEADY STATE PERFORMANCE OF A SKEWED PROPELLER (DTNSRDC 4382 PROPELLER)

To further test the present BEM for more complex problem related to propeller, the steady state flow around a skewed propeller (DTNSRDC 4382 propeller) on an axi-symmetric hub is considered. The particulars of propeller are listed in Table 8.

The DTNSRDC 4382 propeller is a five bladed propeller. The propeller blades are having skew of 36 degrees and the section shape of the blade is a NACA 66 modified thickness form, superimposed on a mean camber line. The geometry of the hub is elliptical. The more details can be found in Cumming *et al.* (1972). Since, the geometry and loading is repeated identically on each of the blades and on each of the hub segments, only one fifth of the geometry needs to be discretized. Only the sixteen span-wise meshes are arranged to be denser towards the tip, and each strip contains 28 upper and lower surface meshes. The mesh arrangement and the body of the propeller are shown in Figure 17a, 17b and 17c.

The wake alignment scheme discussed before is used. Herein, the performance of propeller is computed for 5 different advance ratios. The results are compared with the experimental results of Cumming *et al.* (1972). The measured (Cumming *et al.* (1972)) and computed open water characteristics are shown in Figure 17d and listed in Table 9. The agreement between the experimental and computational results is found to be satisfactory. The pressure distribution for this propeller is also calculated, but due to unavailability of results for comparison these are not presented here. Figure 18c presents the convergence of open water characteristics with respect to number of mesh and we observe that the convergence is achieved with 28 chord-wise and 16 span-wise meshes. Figures 18a and 18b show the convergence of open water characteristics with different wake vortex sheets and for the convergence study two initial wakes with different P/D (0.6 and 1.2) are selected.

Results show that the aligned vortex sheet converges to same sheet irrespective to initial wake sheet. Further, it can be noted that with the aligned wake sheet behind the propeller open water characteristics are well converged, Figure 18d.

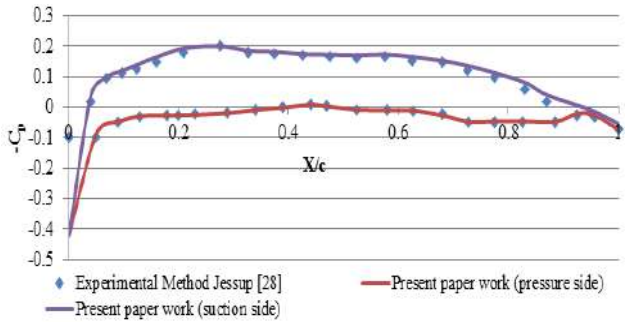

(a) Computed pressure coefficient distribution for DTMB 4119 propeller at r/R =0.7 and J=0.833 and its comparison with Jessup (1989).

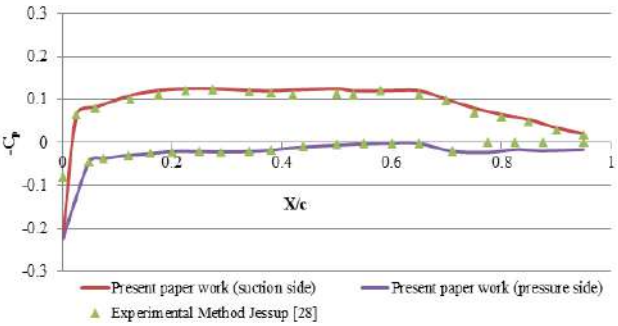

(b) Computed pressure coefficient distribution for DTMB 4119 propeller at r/R =0.9 and J=0.833 and its comparison with Jessup (1989).

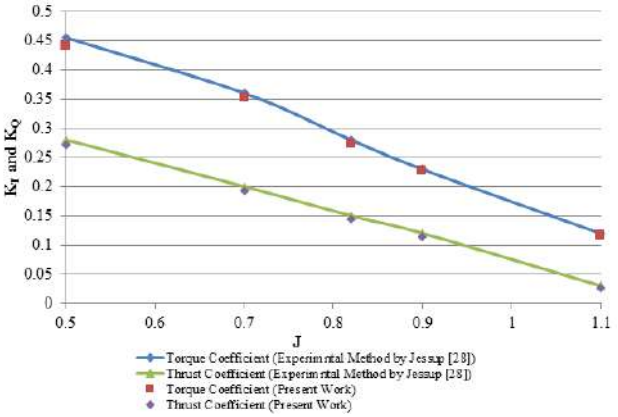

(c) Comparison of the computed open water characteristic of DTMB 4119 propeller by the present BEM based with Jessup (1989).

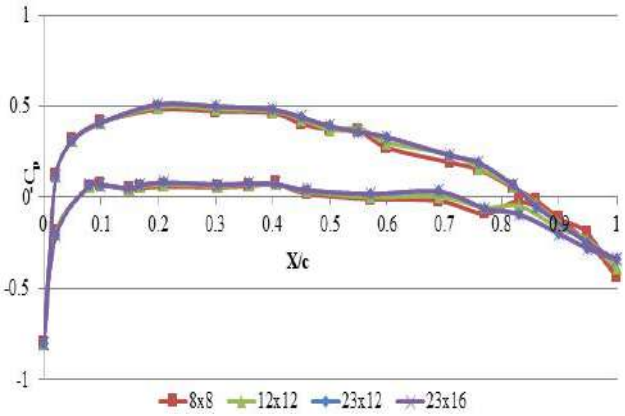

(d) Convergence characteristics of the pressure distribution with different number of panels at r/R=0.3.

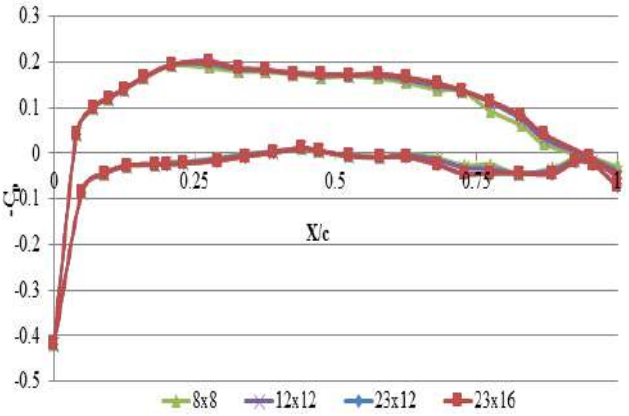

(e) Convergence characteristics of the pressure distribution with different number of panels at r/R=0.7.

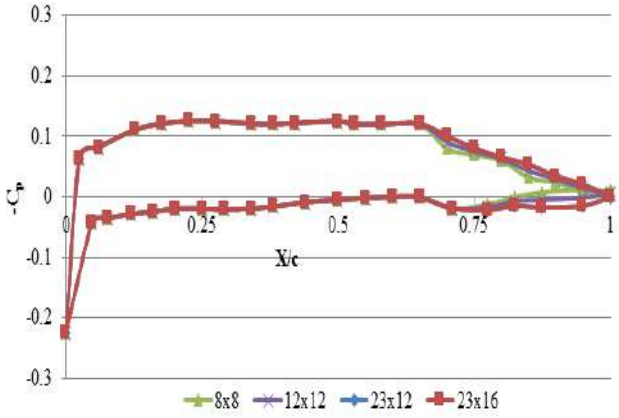

(f) Convergence characteristics of the pressure distribution with different number of panels at r/R=0.9.

Figure 15: Computed pressure coefficient distribution at r/R =0.7 and 0.9 and J=0.833, computed open water characteristic, and convergence characteristics of the pressure distribution with different number of meshes at r/R=0.3, 0.7, and 0.9 and their comparison with Jessup (1989).

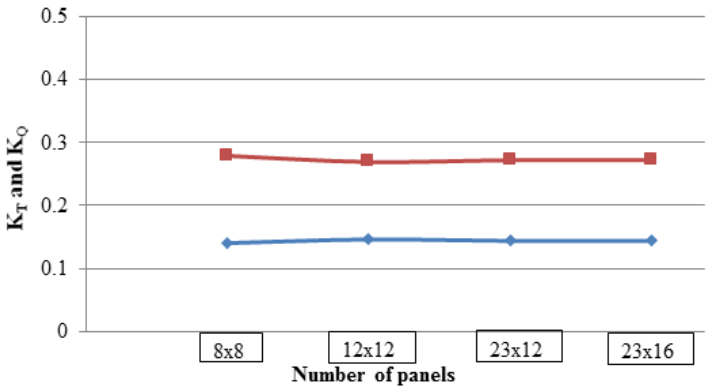

Figure 16: Convergence characteristics of open water characteristics with different number of meshes for the present BEM.

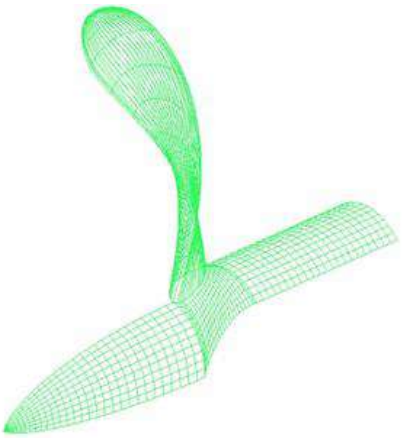

(a) Definition of the geometry and surface panel distribution for DTNSRDC 4382 propeller.

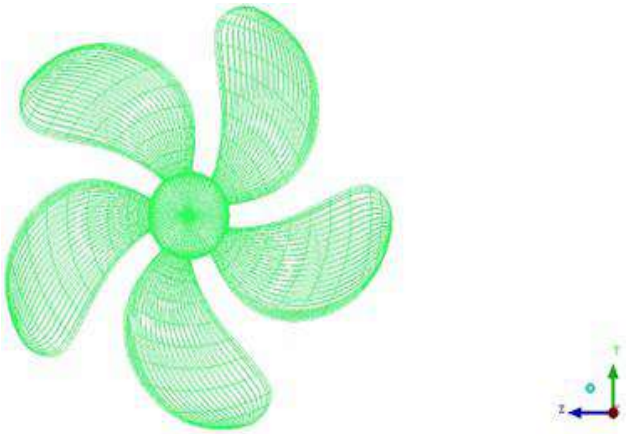

(b) Front view and the surface panel distribution for DTNSRDC 4382 propeller.

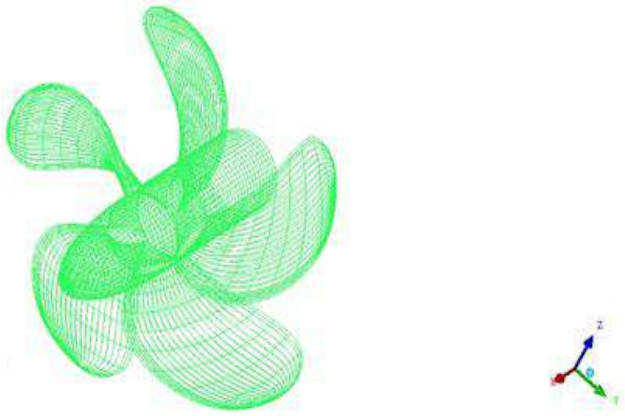

(c) Isometric view and the surface panel distribution for DTNSRDC 4382 propeller.

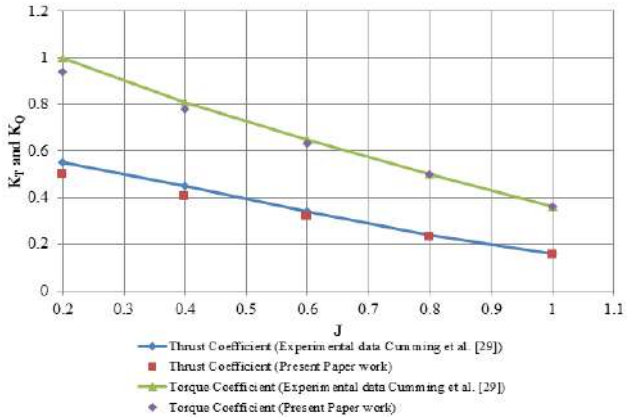

(d) Comparison of the computed open water characteristic of DTNSRDC 4382 propeller by the present BEM with Cumming *et al.* (1972).

Figure 17: Definition of the geometry, surface mesh distribution, front and isometric views and comparison of the computed open water characteristic of DTNSRDC 4382 propeller by the present BEM with Cumming *et al.* (1972).

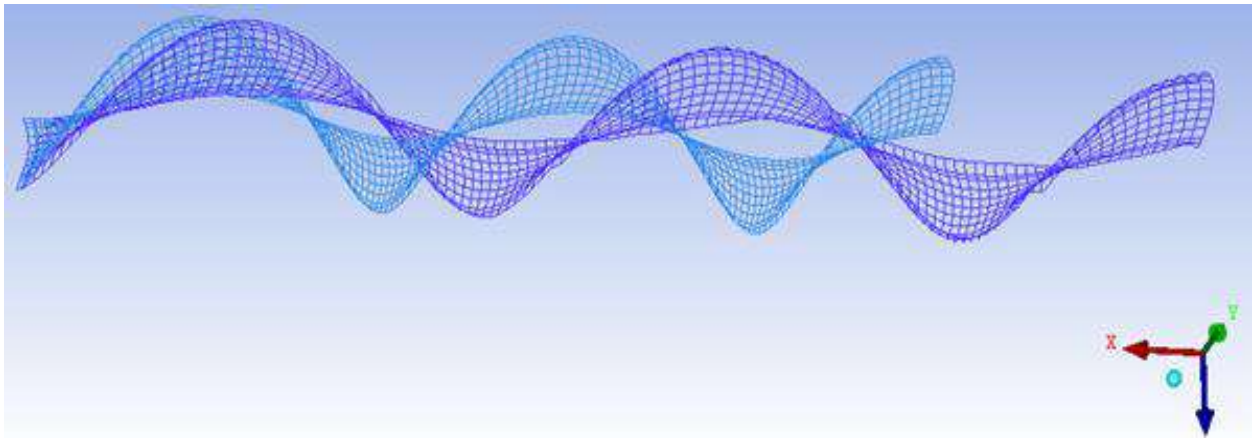

(a) Comparison between the aligned wake starting from initial wake with P/D = 0.6.

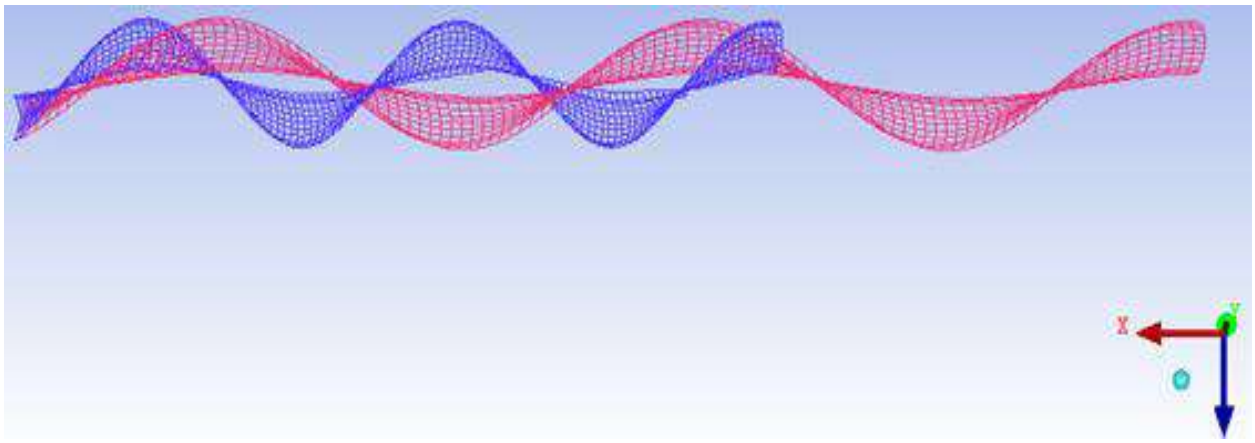

(b) Comparison between the aligned wake starting from initial wake with P/D = 1.2.

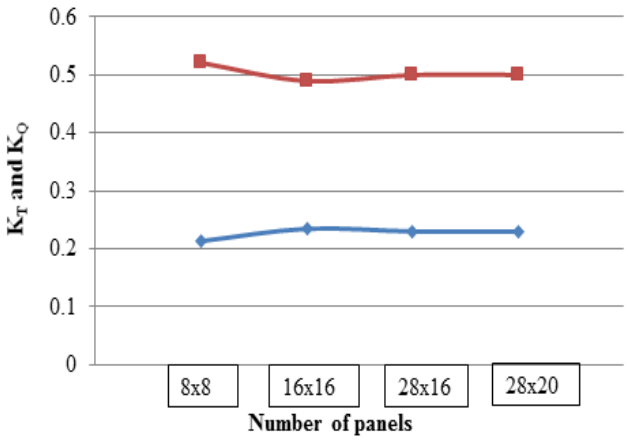

(c) Computational convergence of the open water characteristics with different number of panels of DTNSRDC 4382 propeller by the present BEM.

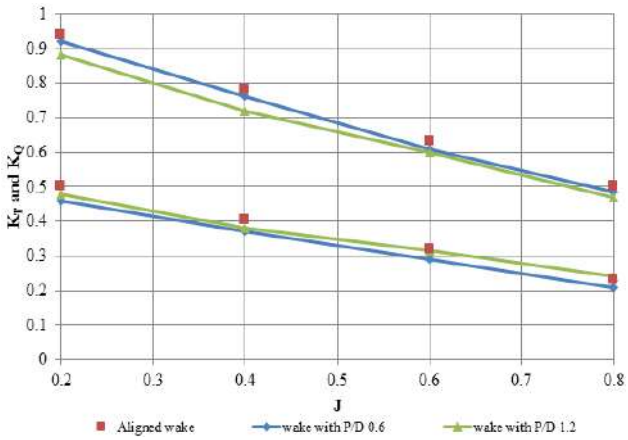

(d) Convergence of the computed open water characteristics with different wake vortex sheets of DTNSRDC 4382 propeller by the present BEM with Cumming *et al.* (1972).

Figure 18: Comparison between the aligned wake starting from initial wake with P/D = 0.6 and 1.2, computational convergence and comparison of the open water characteristics with different number of meshes and with different wake vortex sheets of DTNSRDC 4382 propeller by the present BEM with Cumming *et al.* (1972).

7. CONCLUSIONS AND THE FUTURE SCOPE OF WORK

The present paper has implemented NURBS based iso-geometric approach with the HOPM for the fluid flow analysis on a class of engineering hydrodynamic problems in which fluid flow past the bodies can be studied by Laplace's equation, e.g. subsonic flow around wings, flow around spheres, ellipsoids, and flow past marine propellers. We also studied the CSPM and have shown the superiority of the HOPM over LOPM with an example of the fluid flow around sphere. We studied the FVM in terms of the computational cost involved and compared it with the present BEM for a specific problem and found that the present BEM is superior to the FVM for the problems studied here. This observation is expected to be valid for all types of the 'Boundary Value Problems (BVPs)'. Our presented results studied the effect of the knot vector selection on the body surface representation and the numerical analysis and we have reported ideal choices in terms of knot vector selection. Also, we studied the steady state performance of both the skewed and un-skewed propellers, i.e. DTMB 4119 propeller and DTNSRDC 4382 propeller. Our results have shown that computed pressure distributions on the blade of the marine propeller are in good agreement with the experimental results. Also the open water characteristics of the propeller are in good agreement with the experimental results for the sufficiently high range of the advance coefficients.

Finally, the following main conclusions can be drawn from the present work:

- When viscous effects are not predominant the BEM based present method has a good convergence rate as compared to the FVM (Fluent^{**TM}). For example, in case of the flow around sphere, FVM (Fluent^{**TM}) takes approximately 2.4 times more computational time as compared to the present method (BEM) and also number of elements required by FVM (Fluent^{**TM}) is 5 times more as compared to BEM for same desired accuracy.
- The HOPM converges fast as compared to LOPM, e.g. for the fluid flow over sphere, number of meshes required by LOPM is approximately 10 times more than the number of the meshes required by HOPM for the same desired accuracy.
- The knot vector selection shows a significant effect on both geometry approximation and solution obtained. The centripetal parameter coefficient 'a' around 0.2 gives good accuracy and it seems to be an optional choice.

However, this can only be confirmed with detailed investigation.

- Present method does not show good enough results when viscous effects become predominant. Hence, a viscous correction needs to be implemented and this is to be explored in the future.

Furthermore, we plan to study a NURBS based IGA with implementation of viscous corrections to overcome the shortcomings of potential flow based assumption used in present paper. In addition, limitations of the NURBS can be addressed using the T-splines (Sederberg *et al.* (2003)). Additionally, the weights in the NURBS representation can be optimized which is fairly an open problem as no real solution has been proposed till now. Our future work shall go in these directions and some of them are under investigation.

8. TRADEMARK AND COPYRIGHTS

9. ACKNOWLEDGEMENTS

This research was supported by the internal research grants of IIT Madras, India via a scheme - OE10S007 and a scholarship scheme of the MHRD, GoI, India.

10. REFERENCES

1. ANDERSON, JR. J. D. (2007). *Fundamentals of Aerodynamics*, 4th edition, McGraw-Hill Book Company, USA.
2. ATKINSON, K. E. (1990) *A Survey of Boundary Integral Equation Method for the Numerical Solution of Laplace's Equation in Three Dimensions*, In: Goldberg MA (ed) Numerical solution of integral equations, Plenum Press, USA.
3. BECKER, A. A. (1992). *The Boundary Element Method in Engineering*, McGraw-Hill Book Company, USA.
4. CAO, Y. and BECK, R. (2015). Desingularized boundary integral methods with application in wave hydrodynamics", in the *Proceedings of 34th International Conference on Ocean, Offshore and Arctic Engineering*, St. John's, Newfoundland, Canada, May 31-1 June 5, 2015.
5. CAO, Y., SCHULTZ, W. W. and BECK, R. F. (1991). Three-dimensional desingularized boundary integral methods for potential problems, *Int. J. Num. Meth. Fluids*, 12, pp.785-803.
6. COTTRELL, J. A., HUGHES, T. J. R. and BAZILEVS, Y. (2009). *Isogeometric Analysis: Toward Integration of CAD and FEA*, 1st edition, Wiley, USA.
7. CUMMING, R. A., MORGAN, W. B. and BOSWELL, R. J. (1972). *Highly Skewed Propellers*, Transactions of SNAME, 20, 98-135.
8. DANMEIER, D. G. (1999). *A Higher Order Mesh Method for Large-Amplitude Simulation*

of Bodies in Waves, Ph. D. Thesis, Massachusetts Institute of Technology, USA.

9. DE BOOR, C. (2001). A Practical Guide to Splines, Series on Applied Mathematical Sciences, Springer.
10. FARIN, G. (1999). *NURBS: From Projective Geometry To Practical Use*, 2nd edition, A. K. Peters/CRC Press, USA.
11. GOEL, M. (2016). *Non-Uniform Rational B-Spline (NURBS) Based Iso-Geometric Analysis for Flow Around A Propeller*, Master of Science (By Research) Thesis, Department of Ocean Engineering, IIT Madras, India.
12. HESS, J. L. (1972). *Calculation of Potential Flow About Arbitrary Three Dimensional Lifting Bodies*. McDonnell Douglas report number MDC J5679-01, Oct. 1972, (a somewhat condensed version is contained in *Computer Methods in Applied Mechanics and Engineering*, 2 (1): 1-15.
13. HESS, J. L. (1979). *A Higher Order Mesh Method for Three Dimensional Potential Flow*, Report number NADC 77166-30, Douglas Aircraft Company, USA.
14. HESS, J. L. and SMITH, A. M. O. (1964). *Calculation of Non-Lifting Potential Flow About Arbitrary Three Dimensional Bodies*, Journal of Ship Research, 8 (2): 22-44.
15. HESS, J. L. and VELAREZO, O. W. (1985). *Calculation of Steady Flow About Propellers Using A Surface Mesh Method*, Journal of Propulsion and Power, 1 (6): 470-476.
16. HSIN, C. Y., KERWIN, J. E. and NEWMAN, J. N. (1993). *A Higher-Order Mesh Method Based on B-Splines*, In Proceedings of the 6th International Conference on Numerical Ship Hydrodynamics, Iowa, USA, 133–151.
17. HUGHES, T. J. R. (2012). *The Finite Element Method: Linear, Static and Dynamic Finite Element Analysis*, Courier Dover Publications, USA.
18. HUGHES, T. J. R., COTTRELL, J. A. and BAZILEVS, Y. (2005). *Isogeometric Analysis: CAD, Finite Elements, NURBS, Exact Geometry, and Mesh Refinement*, Computer Methods in Applied Mechanics and Engineering, 194: 4135–4195.
19. JESSUP, S. (1989). *An Experimental Investigation of Viscous Effects of Propeller Blade Flow*, Ph.D. Thesis, The Catholic University of America, USA.
20. JOHNSON, F. T. and RUBBERT, P. E. (1975). *Advanced Mesh Type Influence Coefficient Methods Applied To Subsonic Flows*, 13th AIAA Aerospace Science meeting, Pasadena, California, AIAA paper 75-50 39.
21. KIM, B. K. and NAM, J. H. (1999). *A B-Spline Method Using NURBS Surface*, In 14th International Workshop on Water Waves and Floating Bodies, Port Huron, USA, 76-79.
22. KIM, G. D., LEE, C. S. and KERWIN, J. E. (2007). *A B-Spline Based Higher Order Mesh Method for Analysis of Steady Flow Around Marine Propellers*, Ocean Engineering, 34 (14-15): 2045–2060.
23. KOYAMA, K., KAKUGAWA, A. and OKAMOTO, M. (1986). *Experimental Investigation Of Flow Around A Marine Propeller and Application of Mesh Method to the Propeller Theory*. 16th Symposium on Naval Hydrodynamics, Berkeley, USA.
24. LEE, E. T. Y. (1989). Choosing nodes in parametric curve interpolation, Computer-Aided Design, 21 (6), pp. 363 - 370.
25. LEE, J. T. (1988). *A Potential Based Mesh Method for the Analysis of Marine Propeller in Steady Flow*, Ph.D. Thesis, Department of Ocean Engineering, MIT, USA.
26. LEE, C. H., FARINA, L. and NEWMAN, J. N. (1998). *A Geometry Independent Higher Order Mesh Method and its Application to Wave–Body Interactions*, In Proceedings of Engineering Mathematics and Applications Conference, Adelaide, Australia.
27. LEE, C. S. and KERWIN, J. E. (2003). *A B-Spline Higher-Order Mesh Method Applied to Two Dimensional Lifting Problems*, Journal of Ship Research, 47 (4): 290-298.
28. MANIAR, H. D. (1995). *A Three Dimensional Higher Order Mesh Method Based on B-Spline*, Ph.D. Thesis, Department of Ocean Engineering, MIT, USA.
29. MORINO, L. and KUO, C. C. (1974). *Subsonic Potential Aerodynamics for Complex Configuration: A General Theory*, AIAA Journal, 12 (2): 191-197.
30. PIEGL, L. and TILLER, W. (1996). *The NURBS Book*. 2nd edition, Springer Berlin, Heidelberg, Germany.
31. POZRIKIDIS, C. (2010). *A Practical Guide to Boundary Element Methods with the Software Library BEMLIB*, CRC Press, USA.
32. ROBERTS, A. and RUNDLE, K. (1973). *Computation of First Order Compressible Flow About Wing-Body Configurations*, AERO MA No. 20, British Aircraft Corporation, UK.
33. ROGERS, D. and ADAMS, J. A. (2017). *Mathematical Elements For Computer Graphics*, 2nd edition, McGraw Hill Education, USA.
34. SEDERBERG, T. W., ZHENG, J, BAKENOV, A. and NASRI, A. (2003). *T-splines and T-NURCCSs*. ACM Transactions on Graphic, 22 (3): 477–484.
35. SCHLICHTING, H. (1955). *Boundary Layer Theory*, McGraw-Hill, USA.
36. XU, H. (1992). *A Numerical Study of Fully Nonlinear Water Waves in Three Dimensions*, Ph.D. Thesis, Department of Ocean Engineering, MIT, USA.

APPENDIX - TABLES

Table 1: Propeller offset data of the DTMB 4119 propeller adapted from Jessup (1989).

Offset data parameters: Number of blades: K = 3, Hub diameter ratio: 0.2, Section mean line: NACA a = 0.8, and Thickness distribution: NACA 66 (modified)							
r/R	c/D	x_s/D	$\theta_s(r)$	P/D	t/c	f/c	c
0.20	0.3200	0	0	1.1050	0.2055	0.0143	0.097536
0.30	0.3635	0	0	1.0220	0.1553	0.0232	0.110795
0.40	0.4048	0	0	1.0983	0.1180	0.0230	0.123383
0.50	0.4392	0	0	1.0932	0.0902	0.0218	0.133868
0.60	0.4610	0	0	1.0879	0.0696	0.0207	0.140513
0.70	0.4622	0	0	1.0839	0.0542	0.0200	0.140879
0.80	0.4347	0	0	1.0811	0.0421	0.0197	0.132497
0.90	0.3613	0	0	1.0785	0.0332	0.0182	0.110124
0.95	0.2775	0	0	1.0770	0.0323	0.0163	0.084582
0.98	0.2045	0	0	1.0761	0.0321	0.0145	0.062332
1.00	0.0800	0	0	1.0750	0.0361	0.0188	0.024384

Table 2: Relative error in the adaptive integration.

Number of division	1	4	10	16 ($\chi \leq 0.4$)
Relative error	4.51E-2	7.061E-4	1.2989E-4	1.105E-6

Table 3: Configuration of the computing machine and comparison of the computational cost of the present BEM and Fluent^{**TM} software.

Configuration of the computing machine				
Processor	Intel® Core™ i5-2500 CPU @ 3.30 GHz			
Installed memory (RAM)	16.0 GB			
System type	64-bit Operating system			
Physical memory (Hard disk)	500 GB			
Comparison of the computational cost of the present BEM and Fluent^{**TM} software				
Number of the panels	Computational time for the present BEM	Computational time for the Fluent^{**TM} software	Maximum velocity achieved by the present BEM (cm/s)	Maximum velocity achieved the Fluent^{**TM} software (cm/s)
250	1 min 24 Sec	2 min 04 Sec	1.499102	1.44518
1000	17 min 36 Sec	14 min 23 Sec	1.499772	1.47326
3000	30 min 30 Sec	21 min 36 Sec	1.499982	1.48222
5402	N/A as the sufficient convergence has been achieved already.	49 min 28 sec	N/A as the sufficient convergence has been achieved already.	1.499236

Table 4: Comparison of the computed pressure coefficient on pressure and suction sides for the blade of DTMB 4119 propeller at r/R=0.3 by the present method with the experimental results of Jessup (1989).

(a) Pressure side			
X/c	Experimental value of the pressure coefficient from Jessup (1989)	Numerical solution from the present BEM	Absolute error of the present method w.r.t. the Jessup (1989)
0.000	0.00000	-0.8000	0.80000
0.021	-0.22000	-0.2100	0.01000
0.080	0.08000	0.0700	0.01000
0.100	0.02300	0.0710	0.04800
0.150	0.00861	0.0500	0.04139
0.170	0.08000	0.0700	0.01000
0.210	0.08000	0.0820	0.00200
0.305	0.07000	0.0720	0.00200
0.360	0.07000	0.0770	0.00700
0.405	0.06000	0.0732	0.01320
0.460	0.05000	0.0400	0.01000
0.570	-0.01000	0.0200	0.03000
0.690	-0.02000	0.0320	0.05200
0.770	-0.09800	-0.0600	0.03800
0.830	-0.10000	-0.0920	0.00800
0.900	-0.19000	-0.2000	0.01000
0.950	-0.20000	-0.2800	0.08000
1.000	-0.26000	-0.3400	0.08000
(a) Suction side			
0.021	-0.22	0.1181	0.3381
0.050	0.34	0.3100	0.0300
0.100	0.43	0.4100	0.0200
0.200	0.50	0.5100	0.0100
0.300	0.48	0.5000	0.0200
0.400	0.44	0.4800	0.0400
0.450	0.40	0.4400	0.0400
0.500	0.38	0.3900	0.0100
0.550	0.39	0.3600	0.0300
0.600	0.37	0.3300	0.0400
0.710	0.21	0.2300	0.0200
0.760	0.16	0.1900	0.0300
0.820	0.04	0.0650	0.0250
0.860	-0.01	-0.0500	0.0400
0.950	-0.20	-0.2500	0.0500
1.000	-0.26	-0.3200	0.0600

Table 5: Comparison of the computed pressure coefficient on pressure and suction sides for the blade of DTMB 4119 propeller at r/R=0.7 by the present method with the experimental results of Jessup (1989).

(a) Pressure side			
X/c	Experimental value of the pressure coefficient from Jessup (1989)	Numerical solution from the present BEM	Absolute error of the present method w.r.t. the Jessup (1989)
0.050	-0.10000	-0.08500	0.01500
0.090	-0.05000	-0.04600	0.00400
0.130	-0.03000	-0.02800	0.00200
0.180	-0.02700	-0.02600	0.00100
0.200	-0.02600	-0.02500	0.00100
0.230	-0.02400	-0.02400	0.00000
0.290	-0.01800	-0.01760	0.00040
0.340	-0.00816	-0.00800	0.00016
0.390	0.00000	0.00000	0.00000
0.440	0.01000	0.00980	0.00020
0.470	0.00530	0.00400	0.00130
0.525	-0.00900	-0.00700	0.00200
0.580	-0.01000	-0.00963	0.00037
0.626	-0.01200	-0.01000	0.00200
0.680	-0.02450	-0.02600	0.00150
0.728	-0.05000	-0.04670	0.00330
0.775	-0.04900	-0.04480	0.00420
0.825	-0.05000	-0.04500	0.00500
0.885	-0.05100	-0.04600	0.00500
0.925	-0.02500	-0.02000	0.00500
0.957	-0.03000	-0.02600	0.00400
1.000	-0.07000	-0.07300	0.00300
(a) Suction side			
0.000	-0.098	-0.4200	0.3220
0.040	0.020	0.0400	0.0200
0.070	0.095	0.1000	0.0050
0.098	0.112	0.1200	0.0080
0.125	0.125	0.1400	0.0150
0.160	0.150	0.1650	0.0150
0.210	0.18	0.1930	0.0130
0.275	0.200	0.2000	0.0000
0.327	0.180	0.1850	0.0050
0.375	0.175	0.1820	0.0070
0.425	0.170	0.1740	0.0040
0.475	0.165	0.1720	0.0070
0.525	0.160	0.1700	0.0100
0.575	0.165	0.1730	0.0080
0.625	0.152	0.1650	0.0130
0.680	0.148	0.1520	0.0040
0.725	0.120	0.1360	0.0160
0.775	0.100	0.1125	0.0125
0.830	0.060	0.0800	0.0200
0.870	0.020	0.0400	0.0200
0.950	-0.020	-0.0100	0.0100
1.000	-0.070	-0.0550	0.0150

Table 6: Comparison of the computed pressure coefficient on pressure and suction sides for the blade of DTMB 4119 propeller at r/R=0.9 by the present method with the experimental results of Jessup (1989).

(a) Pressure side			
X/c	Experimental value of the pressure coefficient from Jessup (1989)	Numerical solution from the present BEM	Absolute error of the present method w.r.t. the Jessup (1989)
0.000	-0.0800	-0.22520	0.1452
0.048	-0.0450	-0.04400	0.0010
0.075	-0.0380	-0.03600	0.0020
0.120	-0.0300	-0.02850	0.0015
0.160	-0.0250	-0.02460	0.0004
0.200	-0.0210	-0.01980	0.0012
0.250	-0.0200	-0.02000	0.0000
0.290	-0.0220	-0.02100	0.0010
0.340	-0.0200	-0.01980	0.0002
0.380	-0.0170	-0.01620	0.0008
0.440	-0.0100	-0.00900	0.0010
0.500	-0.0050	-0.00496	4E-05
0.550	-0.0020	-0.00198	2E-05
0.600	-0.0010	-0.00010	0.0009
0.650	-0.0008	-0.00100	0.0002
0.710	-0.0200	-0.01910	0.0009
0.775	0.0000	-0.02200	0.0220
0.825	0.0010	-0.01500	0.0160
0.875	0.0010	-0.01800	0.0190
0.950	0.0010	-0.01500	0.0160
(a) Suction side			
0.025	0.065	0.0640	0.0010
0.060	0.080	0.0820	0.0020
0.125	0.100	0.1100	0.0100
0.175	0.110	0.1210	0.0110
0.225	0.121	0.1252	0.0042
0.275	0.123	0.1250	0.0020
0.340	0.119	0.1210	0.0020
0.380	0.116	0.1200	0.0040
0.420	0.112	0.1220	0.0100
0.500	0.114	0.1250	0.0110
0.530	0.110	0.1200	0.0100
0.580	0.121	0.1200	0.0010
0.650	0.112	0.1202	0.0082
0.700	0.098	0.1000	0.0020
0.750	0.070	0.0800	0.0100
0.800	0.060	0.0650	0.0050
0.850	0.050	0.0530	0.0030
0.900	0.030	0.0340	0.0040
0.950	0.020	0.0200	0.0000

Table 7: Comparison of the computed open water characteristics (K_Q and K_T) of DTMB 4119 propeller by the present BEM with the experimental results of Jessup (1989).

Torque coefficient (K_Q)			
Advance ratio (J)	Experimental values of K_Q from Jessup (1989)	Numerical solution by the present BEM	Absolute error of the present BEM w.r.t. the Jessup (1989)
0.50	0.455	0.4400	0.0150
0.70	0.360	0.3510	0.0090
0.82	0.280	0.2730	0.0070
0.90	0.230	0.2261	0.0039
1.10	0.120	0.1150	0.0050
Thrust coefficient (K_T)			
0.50	0.28	0.27169	0.00831
0.70	0.20	0.19180	0.00820
0.82	0.15	0.14400	0.00600
0.90	0.12	0.11400	0.00600
1.10	0.03	0.02700	0.00300

Table 8: Propeller offset data of the DTNSRDC 4382 propeller adapted from the Cumming *et al.* (1972).

Offset data parameter: Number of blades - K =5, Expanded area ratio 0.725, Hub diameter ratio: 0.2, Section mean line: NACA a=0.8, and Thickness distribution: NACA 66 (modified).					
r/R	$\theta_s(r)$	c/D	t/c	P/D	f/c
0.3	4.6550	0.229	0.1562	1.4332	0.037
0.4	9.3630	0.275	0.1068	1.4117	0.0344
0.5	13.948	0.312	0.0768	1.3613	0.0305
0.6	18.378	0.337	0.0566	1.2854	0.0247
0.7	22.747	0.347	0.0421	1.1999	0.0199
0.8	27.145	0.334	0.0314	1.1117	0.0161
0.9	31.575	0.280	0.0239	1.0270	0.0134
1.0	36.000	0.000	-	0.9420	-

Table 9: Comparison of the computed open water characteristics (K_Q and K_T) of DTNSRDC 4382 propeller by the present BEM with the experimental results of Cumming *et al.* (1972).

Torque co-efficient (K_Q)			
Advance ratio (J)	Experimental values of the K_Q from Cumming *et al.* (1972)	Numerical solution by the present BEM	Absolute error of the present BEM w.r.t. the Cumming *et al.* (1972)
0.2	1.00	0.940	0.060
0.4	0.81	0.780	0.030
0.6	0.65	0.630	0.020
0.8	0.50	0.485	0.015
1.0	0.36	0.350	0.010
Thrust co-efficient (K_T)			
0.2	0.55	0.500	0.050
0.4	0.45	0.405	0.045
0.6	0.34	0.320	0.020
0.8	0.24	0.230	0.010
1.0	0.16	0.155	0.005